

Polaron-driven switching of octupolar order in doped $5d^2$ double perovskite

Dario Fiore Mosca,^{1,2,3} Lorenzo Celiberti,¹ Leonid V. Pourovskii,^{2,3} and Cesare Franchini^{1,4}

¹University of Vienna, Faculty of Physics, Center for Computational Materials Science, Kolingasse 14-16, 1090, Vienna, Austria

²CPHT, CNRS, École polytechnique, Institut Polytechnique de Paris, 91120 Palaiseau, France

³Collège de France, Université PSL, 11 place Marcelin Berthelot, 75005 Paris, France

⁴Department of Physics and Astronomy "Augusto Righi", Alma Mater Studiorum - Università di Bologna, Bologna, 40127 Italy

We investigate how doping-induced small polarons impact the low-temperature multipolar orders of the $5d^2$ double perovskite $\text{Ba}_2\text{CaOsO}_6$. By computing intersite exchange interactions between $5d^1$ localized hole polarons and $5d^2$ magnetic ions from first principles, we demonstrate the reversal of the dominant octupolar exchange from ferromagnetic to antiferromagnetic. Solving the corresponding effective Hamiltonian we find this reversal to account for the progressive suppression of the ferro-octupolar order and the reduction of the ordering temperature upon Na doping. These findings clarify previously ambiguous experimental observations and demonstrate that charge doping in the form of small polarons offers a viable route to tuning intersite exchange interactions in spin-orbit-entangled materials, enabling the emergence of novel quantum orders.

Transition metal oxides with $4d$ and $5d$ magnetic ions have reshaped our understanding of strong spin-orbit (SO) coupled physics in condensed matter [1]. These systems exhibit a wide range of phenomena, from the SO-assisted Mott insulating phase in Iridates [2] to non-trivial topology [3] and possible Kitaev quantum spin liquids [4]. In particular, cubic double perovskites (DPs) containing $5d^1$ and $5d^2$ ions have attracted interest in the past years due to the ordering of high-rank multipoles that, although being detected experimentally, via e.g. thermodynamic measurements, defy precise identification due to the "blindness" of local probes [5, 6]. High-rank multipoles in DPs stem from SO entanglement of the spin S with the effective t_{2g} orbital angular momentum $l = 1$ on the $5d$ shell. The corresponding ground state multiplet (GSM), defined by the effective total angular momentum $J_{\text{eff}} = S + l$, can therefore host multipolar moments up to rank $K = 2J_{\text{eff}}$ [6, 7].

Different occupation of the magnetic ion lead to distinct scenarios. In the case of $5d^1$, one finds $J_{\text{eff}} = 3/2$ GSM that can be further split in two Kramers doublets by distortions of the cubic lattice. This scenario is exemplified by $\text{Ba}_2\text{NaOsO}_6$, where nuclear magnetic resonance (NMR) measurements revealed two distinct phase transitions as the temperature decreases [8]. The first transition, occurring around $T_q \sim 10$ K and often referred to as "broken local point symmetry" (BLPS) phase, involves a structural distortion of the Os-O octahedra from cubic to lower symmetry, accompanied by the ordering of electric quadrupoles [8]. The second transition, detected at $T_N \sim 7$ K from both magnetization measurements, muon spin resonance (μSR) and NMR, is attributed to the onset of a canted antiferromagnetic phase with net ferromagnetic moment aligned along the $[110]$ direction [8, 9]. Despite clear evidence from NMR, the exact nature of the BLPS phase remains elusive, as other experimental techniques have struggled to detect or characterize

it [10–12], such that recent works proposed a dynamical Jahn-Teller effect as explanation for this apparent contradiction [13, 14].

$\text{Ba}_2\text{CaOsO}_2$, as well as isoelectronic $5d^2$ osmates of the same family, present an equally intriguing puzzle. They exhibit a single phase transition into a state that breaks time-reversal symmetry (TRS), while lacking observable dipole magnetic moments and maintaining the cubic $\text{Fm}\bar{3}\text{m}$ symmetry [15–18]. In these systems, the $J_{\text{eff}} = 2$ GSM is split by a "remnant" octahedral CF (rcf) in an E_g non-Kramers doublet well separated in energy (10–20 meV) from the excited T_{2g} triplet (See Figure 1). The E_g doublet lacks a dipolar moment but can host quadrupolar and octupolar moments. Theoretical and experimental works on $5d^2$ cubic osmates propose conflicting order parameters: either an antiferro ordering of electric quadrupoles (AFQ) [19, 20], which would break cubic symmetry while preserving TRS, or a ferro-

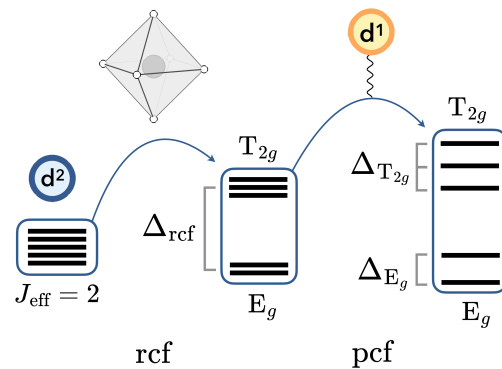


FIG. 1: Evolution of the fivefold degenerate d^2 GSM with $J_{\text{eff}} = 2$ (left) under "remnant" octahedral crystal field (rcf) with $T_{2g} - E_g$ triplet-doublet splitting (middle) and polaron crystal field (pcf) acting on the non-Kramers levels causing a further splitting (right).

ordering of magnetic octupoles (\mathcal{FO}) [15, 18, 21–24]. The latter providing a more consistent description of the experimental findings [15].

In this context, Cong and coworkers [25] obtained valuable data on the doping-driven transition from $5d^1$ to $5d^2$ in $\text{Ba}_2\text{Ca}_{1-\delta}\text{Na}_\delta\text{OsO}_6$ using magnetization measurements, μSR and NMR. They find the BLPS phase across all NMR-accessible Na concentrations followed, upon lowering the temperature, by a region of broken TRS, with the corresponding transition temperature T_o increasing as $\delta \rightarrow 0$. The persistence of the BLPS phase is ascribed to AFQ ordering, suggested to coexist with AFM order up to $\delta = 0.1$. However, this interpretation conflicts with the full Ca limit ($\delta = 0$), where the E_g doublet forbids dipole moments and where the mutual exclusivity of AFQ and \mathcal{FO} phases leaves the origin of the broken TRS region unresolved.

From a theoretical perspective, Voleti and coworkers [26] applied a Density Functional Theory (DFT) framework to $\text{Ba}_2\text{Ca}_{1-\delta}\text{Na}_\delta\text{OsO}_6$ finding that strain fields generated by dopant Na ions in the small $\delta \rightarrow 0$ limit suppress the \mathcal{FO} transition temperature. Clusters of neighboring impurities are predicted to induce “parasitic” dipole moments on adjacent sites through T_{2g} strain fields. While these results offer valuable insight into the effects of local strain on the \mathcal{FO} phase [23, 26], they do not account for the reported formation of small polarons, which underlies the coexistence of different J_{eff} states [27].

Small polarons are quasiparticles arising from the lattice-assisted trapping of dopant charges [28]. In $\text{Ba}_2\text{Ca}_{1-\delta}\text{Na}_\delta\text{OsO}_6$ they promote the localization of states with distinct $5d^1$ and $5d^2$ electronic configurations, while keeping the system insulating at all δ [27]. Though mobile at high temperatures, they become static at the temperatures relevant to multipolar orders. Hence, a set of static $5d^1$ polarons coupled by intersite exchanges to a matrix of $5d^2$ ions can give rise to novel ordered phases.

In this Letter we investigate the interplay of polarons and multipolar orders in $\text{Ba}_2\text{Ca}_{1-\delta}\text{Na}_\delta\text{OsO}_6$ close to the $5d^2$ limit ($\delta \leq 0.25$). Using a fully *ab initio* approach, we derive the microscopic Hamiltonian, incorporating mixed intersite exchange interactions (IEI) between $J_{\text{eff}} = 3/2$ and $J_{\text{eff}} = 2$ GSMs while accounting for CF and (hole) doping effects. Our key finding is that the dominant IEI between $5d^1$ polarons and the $5d^2$ matrix is actually antiferro-octupolar (AFQ), resulting in the occurrence of AFQ polaronic moments within the broader \mathcal{FO} order. This octupolar reversal at the polaronic site is accompanied by small dipole moments appearing on its neighboring sites. The sign reversal stems from the distinct physical representations in the one-electron and two-electron manifolds of the relevant local operators in the t_{2g} space having opposite signs. The consequence is a sign change of $d^2 - d^1$ IEI with respect to the same coupling between ions of the same occupancy. Our predicted ordering tem-

peratures show very good agreement with experimental measurements, particularly when the effects of polaron-induced structural distortions are included.

Effective Hamiltonian. The effective Hamiltonian of $\text{Ba}_2\text{Ca}_{1-\delta}\text{Na}_\delta\text{OsO}_6$ is specified by

$$H^{J_{\text{eff}}} = \sum_{\langle ij \rangle} \sum_{K_i K_j} V_{K_i K_j}^{QQ'}(ij) O_{K_i}^Q(i) O_{K_j}^{Q'}(j) + \sum_i H_{rcf}^i + \sum_{i \in \text{pol}_{NN}} H_{pcf}^i. \quad (1)$$

Here the first summation (ij) runs over the Os-Os bond, the second over the multipolar momenta of the ranks $K_i, K_j' = 1, 2, 3$ for $J_{\text{eff}} = 3/2$ (and 4 for $J_{\text{eff}} = 2$) with projections Q, Q' . The labels K_i/K_j represent the total angular momentum and site-dependent ranks $K(J_i)/K(J_j)$ respectively, consequence of the site-specific GSM. For simplicity, we will omit the i/j subscripts from now on. Finally, $H_{rcf}^i = V_{rcf}[O_4^0(i) + 5O_4^4(i)]$ is the rcf Hamiltonian, while $H_{pcf}^i = B_2^0 O_2^0(i) + B_2^2 O_2^2(i)$ is the polaron crystal field Hamiltonian induced by the localized d^1 charge on neighboring polaronic sites (See Figure 1).

The J_{eff} -IEI constants $V_{KK'}^{QQ'}(ij)$ are calculated with the Force-Theorem in Hubbard-I (FT-HI) approach [29]. The FT-HI derives J_{eff} -IEI from the converged paramagnetic electronic structure obtained by DFT [30] + dynamical mean-field theory [31–34] in the Hubbard-I (HI) approximation [35]. We employ the latest version of the publicly available MagInt code, which implements the FT-HI IEI calculations for different electronic configurations and correlated environments [36]. The method and computational setup are detailed in the Supplemental Material (SM) [37].

Polaron modeling in DFT+HI and crystal fields. Doping at low d^1 concentration is modeled by employing the tetragonal supercell depicted in Figure 2a, containing 8 f.u.. To disentangle structural effects from polaronic ones, we adopt the cubic structure of the pristine d^2 compound of Ref. [16] and account for hole-doping via the virtual crystal approximation. Calculations including explicit chemical substitution for the same structure yield consistent results (see SM [37]).

We find that the overall level structure arising from CF and SO effect is reproduced for both d^1 and d^2 sites. On the d^1 site the calculated CF and SO splittings are found to be ≈ 4.65 eV and ≈ 0.46 eV respectively, in good agreement with X-ray absorption near edge structure results and previous *ab initio* works [12, 38]. On the d^2 sites the calculated rcf splitting of the $J_{\text{eff}} = 2$ GSM is found to be $\Delta_{rcf} \approx 19$ meV, in very good agreement with specific heat measurements and previously reported DFT+HI calculations [15, 21, 24]. Both the E_g and T_{2g} manifolds undergo additional splittings induced

by the polaron, which lowers the local O_h symmetry. These pcf splittings depend on their orientation relative to the d^1 site: out-of-plane splittings reach $\Delta_{E_g} \sim 5$ meV and $\Delta_{T_{2g}} \sim 2$ meV, compared to in-plane values $\Delta_{E_g} \approx \Delta_{T_{2g}} \sim 1$ meV. Additional details, wavefunctions and CF parameters are provided in the SM [37].

Octupolar switching and its microscopic origin. Our calculated diagonal exchange constants V_{KK}^{QQ} are presented in Fig. 2b for $d^2 - d^2$ and $d^1 - d^2$ interacting bonds, as illustrated in Fig. 2a, with the full J_{eff} -IEI matrices reported in the SM [37]. As expected, mapping the $d^2 - d^2$ J_{eff} -IEI onto the low-lying E_g subspace yields a dominant octupole–octupole interaction, $V_{33}^{22} \equiv V^{xyz}$, in full agreement with the pristine d^2 compound [24]. However, a striking difference arises in the presence of polarons: while this coupling remains ferromagnetic for all $d^2 - d^2$ bonds, it reverses sign and turns antiferromagnetic for $d^1 - d^2$ bonds. This switching of the dominant multipolar channel demonstrates how the introduction of d^1 polarons reshapes the exchange landscape at a fundamental level, providing a microscopic origin for the destabilization of FO order and paving the way for competing

multipolar phases.

To clarify the origin of this sign reversal, we perform a DFT+HI calculation without SO coupling in the spin+orbital t_{2g} basis. The corresponding effective multipolar t_{2g} -Hamiltonian is written as:

$$H^{t_{2g}} = \sum_{\langle ij \rangle} \sum_{\substack{ss', ll' \\ \alpha\alpha', \beta\beta'}} I_{ss', ll'}^{\alpha\alpha', \beta\beta'}(ij) \tau_{s, l}^{\alpha, \beta}(i) \tau_{s', l'}^{\alpha', \beta'}(j), \quad (2)$$

where the second summation runs over the spin (s, s') and orbital (l, l') ranks with components (α, α') and (β, β') respectively, $\tau_{s, l}^{\alpha, \beta} = S_s^\alpha \otimes L_l^\beta$ are normalized spin+orbital multipolar operators [6]. The t_{2g} -shell-mediated IEI couplings (t_{2g} -IEI) $I_{ss', ll'}^{\alpha\alpha', \beta\beta'}(ij)$ were computed within the FT-HI approach.

Although the t_{2g} -IEI are not straightforward to interpret, they can be linked to the $V_{KK}^{QQ'}$ by SO-projection onto the J_{eff} many-electron bases. Specifically, we find that the relevant t_{2g} -IEI contributing to V^{xyz} are the diagonal $I_{11, 22}^{zz, (xy)(xy)}$ terms, coupling dipole spin (z) and orbital quadrupole (xy), and corresponding permutations ($\alpha=x, \beta=yz$), ($\alpha=y, \beta=xz$).

Our SO-projection reproduces the correct sign of all J_{eff} -IEI for both $d^2 - d^2$ and $d^1 - d^2$ bonds, but with reduced magnitude beyond dipole–dipole terms, likely due to neglecting of SOC in excited d^1 and d^3 states. Crucially, the sign reversal between $d^1 - d^2$ and $d^2 - d^2$ bonds already appears in the $I_{11, 22}^{\alpha\alpha, \beta\beta}$ couplings, showing that this effect is not induced by SO coupling. Specifically, it originates from the different representations of the one-electron t_{2g} -shell operators in the many-electron d^1 and d^2 bases: the one-electron t_{2g} -shell operators with ($s = 1, l = 2$) acquire a minus sign when expressed in the d^2 many-electron Hilbert space. This sign switch is compensated on $d^2 - d^2$ bonds but remains explicit on $d^1 - d^2$ ones (see End Matter for the detailed derivation).

Lastly, to clarify the physical meaning of the spin+orbital $\tau_{s, l}^{\alpha, \beta}$ operator, we express $\tau_{0, 2}^{0, \beta}$ in terms of one-electron occupancy operators $n_{\gamma, \delta}$ of the t_{2g} shell, as is standard in model Hamiltonian methods [39–42]. We find $\tau_{0, 2}^{0, xy} \propto n_{xz, yz} + n_{yz, xz}$ with $n_{yz, xz} = i(c_{yz}^\dagger c_{xz} - c_{xz}^\dagger c_{yz})$, highlighting the role of intra-orbital mixing in the emergence of high-rank multipolar phases.

Ordered phase. We solve the full effective Hamiltonian of Eq. 1, incorporating both d^1 and d^2 sites, within the single site mean field (MF) approximation using the “McPhase” package [43] together with an in-house module. To simplify the treatment of mixed-valence interactions, we exclude the couplings to hexadecapole operators ($K = 4$) present in both $d^1 - d^2$ and $d^2 - d^2$ J_{eff} -IEI, as these contributions are expected to be negligible.

We find two second-order phase transitions occurring at $T_o \sim 93$ K and $T \sim 4$ K. While we do not discuss the latter in detail here, as its very low temperature in MF

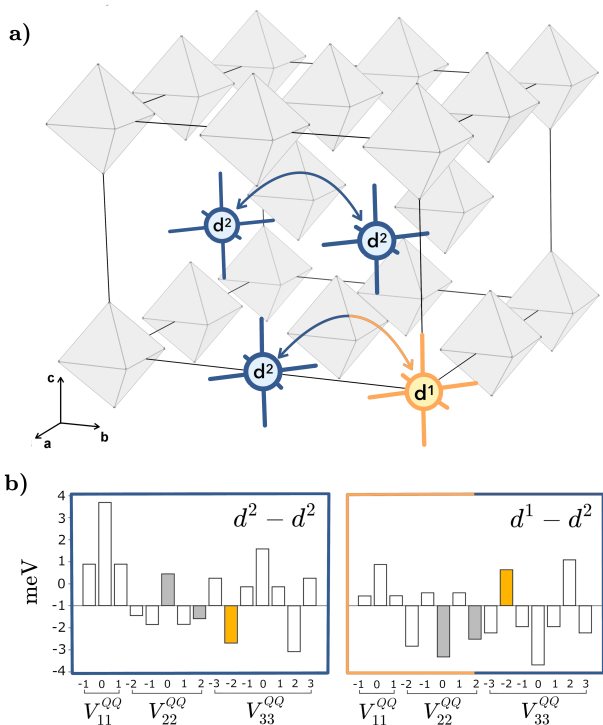


FIG. 2: a) The polaronic supercell used. The IE paths connecting the $d^2 - d^2$ and $d^1 - d^2$ are marked by blue and blue/orange arrows. b) Corresponding diagonal IEI V_{KK}^{QQ} . The active components within the E_g GSM are indicated by filled colored bins and the octupole–octupole IE V^{xyz} is highlighted in yellow. The full IEI matrices are given in the SM [37].

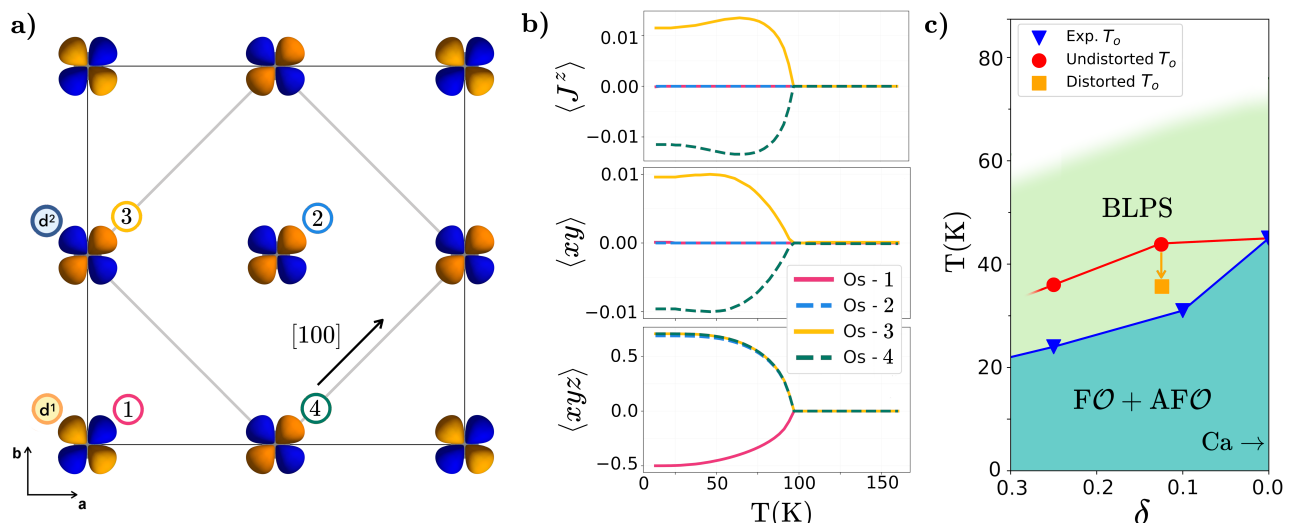


FIG. 3: a) $F\mathcal{O}$ and $AF\mathcal{O}$ order in $Ba_2Ca_{1-\delta}Na_\delta OsO_6$ in the supercell used (top view). The labels 1-4 are related to the sub-figure b), where the MF values of dipole J^z , quadrupole xy and octupole xyz are shown as function of temperature. c) Evolution of the ordering temperature T_o with doping for the experimental data (blue triangles) and the undistorted cubic structure (red circles). The temperature shift at $x = 0.125$ arising from polaronic structural distortions is indicated by the orange square.

makes it less significant, additional details are provided in the SM [37]. The first transition is noteworthy and leads to a complex order that combines a $F\mathcal{O}$ order of xyz octupoles on all sites except on the polaronic one, where the xyz octupole is $AF\mathcal{O}$ ordered (See Figure 3a). Additionally, the polaronic nearest neighbors in the ab -plane develop small AF magnetically ordered dipole moments of $\approx 0.01\mu_B$. These are oriented along the z -axis and accompanied by the ordering of t_{2g} electric quadrupoles with xy character (see Figure 3b for the MF values).

Thus, both T_{2g} distortions induced by dopants [23] and polaronic charges alter the $J_{\text{eff}} = 2$ CF to an extent that parasitic dipole moments emerge. Interestingly, despite the stronger out-of-plane $\Delta_{T_{2g}}$ splitting compared to the in-plane one, no dipoles form on the out-of-plane sites. This is attributed to the ground-state wavefunctions, which do not couple to the first T_{2g} excited state via the z -dipole operator (see SM [37]).

It is worth noting that within the $5d^1$ $J_{\text{eff}} = 3/2$ manifold all multipolar degrees of freedom are, in principle, active and can order. Our results demonstrate that the rcf on the d^2 sites quenches all multipolar IE channels except those allowed within the E_g doublet, thereby imposing an "effective" CF on the polaronic site.

Ordering Temperature evolution We investigate how hole doping affects the transition temperature in $Ba_2Ca_{1-\delta}Na_\delta OsO_6$. The outcome is not obvious a priori: although the $d^1 - d^2$ J_{eff} -IEI interactions can be up to $\sim 80\%$ weaker than in the pristine d^2 case [24], the V^{xyz} coupling remains comparable (see the SM [37]). To track

the evolution of the ordering temperature, we compute the J_{eff} -IEI at higher Na concentration $\delta = 0.25$.

The model averages two polaronic geometries, with the extra d^1 charge residing either in-plane (next-nearest neighbor) or out-of-plane (nearest neighbor). The corresponding MF solutions contain two $AF\mathcal{O}$ ordered polarons in both cases, confirming the robustness of octupolar order against charge doping at these low Na concentrations. After rescaling the MF values to match the experimental T_o at $\delta = 0$, we find that the undistorted results already reproduce the overall experimental trend (Fig. 3c, red circles). The reduction of T_o upon doping arises from a subtle interplay of several factors: polaron-induced changes in the $E_g - T_{2g}$ rcf splittings, modifications of the pcf at higher δ , slightly weakened xyz IE and the different multiplicity of the magnetic ion's GSs within the supercell (see End Matter).

Structural distortions are also expected to play an essential role, since polaron localization necessarily involves local lattice relaxation. To examine this effect, we performed a full relaxation of the structure for $\delta = 0.125$ using the Vienna Ab Initio Simulation Package (VASP) [44] within the constrained DFT+U method. The on-site density matrices were initialized with the combined $F\mathcal{O} + AF\mathcal{O}$ configuration, as obtained at DFT+HI level. The approach, detailed in Ref. [45] and summarized in the SM, showed to accurately capture high-rank multipolar phases in DFT. From the optimized distorted structure we computed both J_{eff} -IEI and ground state properties in FT-HI.

The MF calculation reproduce the previously identi-

fied AF \mathcal{O} polaron embedded in the F \mathcal{O} matrix, albeit with stronger parasitic dipole moments, now distributed across all osmium sites (see SM [37]). Moreover, we find that including polaron-induced structural effects improves the agreement with experiment by a large extent (Fig.3c, orange square). It is therefore reasonable to expect that chemical substitution and a more complex treatment of Na dopant configurations, as examined in Ref [26], could lead to an even closer quantitative agreement with the experimental data.

Conclusions. To bridge the distinct physical regimes of $5d^1$ and $5d^2$ double perovskites and connect their different J-effective multipolar phases, we derived and solved from first principles the effective Hamiltonian of $\text{Ba}_2\text{Ca}_{1-\delta}\text{Na}_\delta\text{OsO}_6$, explicitly accounting for polaronic charges at low Na-doping levels through material-specific DFT calculations. Our analysis demonstrates a polaron-induced reversal of the dominant octupolar exchange, originating from different representation of t_{2g} -shell spin+orbital operators in one-electron and two-electron bases. This reversal of the octupolar IEI provides direct evidence for a coupling between polaronic degrees of freedom and magnetic interactions, an effect not previously reported. Beyond explaining the experimentally observed suppression of the ordering temperature with doping, this result opens a pathway to designing and controlling novel quantum orders in spin-orbit systems through charge doping.

Support by the the Austrian Science Fund (FWF) grant J4698 is gratefully acknowledged. D. F. M. and L. C. thank the computational facilities of the Austrian Scientific Computing (ASC). L. V. P. acknowledges the support by CNRS through the Tremplin@Physique 2025 program and by the CPHT computer team. The authors thank the Erwin Schrödinger Institute (ESI) for hosting the ESI-PsiK workshop ‘Spin-orbit entangled quantum magnetism’ and all participants for the many enlightening discussions.

[1] William Witczak-Krempa, Gang Chen, Yong Baek Kim, and Leon Balents, “Correlated quantum phenomena in the strong spin-orbit regime,” *Annual Review of Condensed Matter Physics* **5**, 57–82 (2014).

[2] B. J. Kim, Hosub Jin, S. J. Moon, J.-Y. Kim, B.-G. Park, C. S. Leem, Jaejun Yu, T. W. Noh, C. Kim, S.-J. Oh, J.-H. Park, V. Durairaj, G. Cao, and E. Rotenberg, “Novel $J_{\text{eff}} = 1/2$ Mott state induced by relativistic spin-orbit coupling in Sr_2IrO_4 ,” *Phys. Rev. Lett.* **101**, 076402 (2008).

[3] Jairo Sinova, Sergio O. Valenzuela, J. Wunderlich, C. H. Back, and T. Jungwirth, “Spin hall effects,” *Rev. Mod. Phys.* **87**, 1213–1260 (2015).

[4] G. Jackeli and G. Khaliullin, “Mott insulators in the

strong spin-orbit coupling limit: From Heisenberg to a quantum compass and Kitaev models,” *Phys. Rev. Lett.* **102**, 017205 (2009).

[5] Leonid V. Pourovskii, Dario Fiore Mosca, Lorenzo Celiberti, Sergii Khmelevskiy, Arun Paramekanti, and Cesare Franchini, “Hidden orders in spin-orbit-entangled correlated insulators,” *Nature Reviews Materials* (2025), 10.1038/s41578-025-00824-z.

[6] P. Santini, S. Carretta, G. Amoretti, R. Caciuffo, N. Magnani, and G. H. Lander, “Multipolar interactions in f -electron systems: The paradigm of actinide dioxides,” *Rev. Mod. Phys.* **81**, 807–863 (2009).

[7] Y. Kuramoto, H. Kusunose, and A. Kiss, “Multipole orders and fluctuations in strongly correlated electron systems,” *Journal of the Physical Society of Japan* **78**, 072001 (2009).

[8] L Lu, M. Song, W. Liu, A. P. Reyes, P. Kuhns, H. O. Lee, I. R. Fisher, and V. F. Mitrović, “Magnetism and local symmetry breaking in a Mott insulator with strong spin orbit interactions,” *Nature Communications* **8**, 14407 (2017).

[9] D. Fiore Mosca, L V. Pourovskii, B. H. Kim, P. Liu, S. Sanna, F. Boscherini, S. Khmelevskiy, and C. Franchini, “Interplay between multipolar spin interactions, jahn-teller effect, and electronic correlation in a $J_{\text{eff}} = \frac{3}{2}$ insulator,” *Phys. Rev. B* **103**, 104401 (2021).

[10] A. S. Erickson, S. Misra, G. J. Miller, R. R. Gupta, Z. Schlesinger, W. A. Harrison, J. M. Kim, and I. R. Fisher, “Ferromagnetism in the Mott insulator $\text{Ba}_2\text{NaOsO}_6$,” *Phys. Rev. Lett.* **99**, 016404 (2007).

[11] V. da Cruz Pinha Barbosa, J. Xiong, P. M. Tran, M. A. McGuire, J. Yan, M. T. Warren, R. V. Aguilar, W. Zhang, M. Randeria, N. Trivedi, D. Haskel, and P. M. Woodward, “The impact of structural distortions on the magnetism of double perovskites containing $5d^1$ transition-metal ions,” *Chemistry of Materials* **34**, 1098–1109 (2022).

[12] Jagadesh Kopula Kesavan, Dario Fiore Mosca, Samuele Sanna, Francesco Borgatti, Götz Schuck, Phuong Minh Tran, Patrick M. Woodward, Vesna F. Mitrović, Cesare Franchini, and Federico Boscherini, “Doping evolution of the local electronic and structural properties of the double perovskite $\text{Ba}_2\text{Na}_{1-x}\text{Ca}_x\text{OsO}_6$,” *The Journal of Physical Chemistry C* **124**, 16577–16585 (2020).

[13] S. Agrestini, F. Borgatti, P. Florio, J. Frassinetti, D. Fiore Mosca, Q. Faure, B. Detlefs, C. J. Sahle, S. Francoual, J. Choi, M. Garcia-Fernandez, K.-J. Zhou, V. F. Mitrović, P. M. Woodward, G. Ghiringhelli, C. Franchini, F. Boscherini, S. Sanna, and M. Moretti Sala, “Origin of magnetism in a supposedly nonmagnetic osmium oxide,” *Phys. Rev. Lett.* **133**, 066501 (2024).

[14] N. Iwahara and L F. Chibotaru, “Vibronic order and emergent magnetism in cubic d^1 double perovskites,” *Phys. Rev. B* **107**, L220404 (2023).

[15] D. D. Maharaj, G. Sala, M. B. Stone, E. Kermarrec, C. Ritter, F. Fauth, C. A. Marjerrison, J. E. Greedan, A. Paramekanti, and B. D. Gaulin, “Octupolar versus Néel order in cubic $5d^2$ double perovskites,” *Phys. Rev. Lett.* **124**, 087206 (2020).

[16] C M Thompson, J P Carlo, R Flacau, T Aharen, I A Leahy, J R Pollicemi, T J S Munsie, T Medina, G M Luke, J Munevar, S Cheung, T Goko, Y J Uemura, and J E Greedan, “Long-range magnetic order in the $5d^2$ double perovskite $\text{Ba}_2\text{CaOsO}_6$: comparison with spin-

- disordered Ba_2YReO_6 ,” *Journal of Physics: Condensed Matter* **26**, 306003 (2014).
- [17] C. A. Marjerrison, C. M. Thompson, G. Sala, D. D. Maharaj, E. Kermarrec, Y. Cai, A. M. Hallas, M. N. Wilson, T. J. S. Munsie, G. E. Granroth, R. Flacau, J. E. Greedan, B. D. Gaulin, and G. M. Luke, “Cubic $\text{Re}6+$ ($5d1$) double perovskites, $\text{Ba}_2\text{MgReO}_6$, $\text{Ba}_2\text{ZnReO}_6$, and $\text{Ba}_2\text{Y}_{2/3}\text{ReO}_6$: Magnetism, heat capacity, μSR , and neutron scattering studies and comparison with theory,” *Inorganic Chemistry* **55**, 10701–10713 (2016).
- [18] J. Okamoto, G. Shibata, Yu. S. Ponomov, H. Hayashi, K. Yamaura, H. Y. Huang, A. Singh, C. T. Chen, A. Tanaka, S. V. Streltsov, D. J. Huang, and A. Fujimori, “Spin-orbit-entangled state of $\text{Ba}_2\text{CaOsO}_6$ studied by O K-edge resonant inelastic X-ray scattering and Raman spectroscopy,” *npj Quantum Materials* **10**, 44 (2025).
- [19] Giniyat Khaliullin, Derek Churchill, P. Peter Stavropoulos, and Hae-Young Kee, “Exchange interactions, Jahn-teller coupling, and multipole orders in pseudospin one-half $5d^2$ Mott insulators,” *Phys. Rev. Research* **3**, 033163 (2021).
- [20] Derek Churchill and Hae-Young Kee, “Competing multipolar orders in a face-centered cubic lattice: Application to the osmium double perovskites,” *Phys. Rev. B* **105**, 014438 (2022).
- [21] A. Paramekanti, D. D. Maharaj, and B. D. Gaulin, “Octupolar order in d -orbital Mott insulators,” *Phys. Rev. B* **101**, 054439 (2020).
- [22] Sreekar Voleti, D. D. Maharaj, B. D. Gaulin, Graeme Luke, and A. Paramekanti, “Multipolar magnetism in d -orbital systems: Crystal field levels, octupolar order, and orbital loop currents,” *Phys. Rev. B* **101**, 155118 (2020).
- [23] Sreekar Voleti, Arijit Haldar, and Arun Paramekanti, “Octupolar order and ising quantum criticality tuned by strain and dimensionality: Application to d -orbital Mott insulators,” *Phys. Rev. B* **104**, 174431 (2021).
- [24] L. V. Pourovskii, D. Fiore Mosca, and C. Franchini, “Ferro-octupolar order and low-energy excitations in d^2 double perovskites of osmium,” *Phys. Rev. Lett.* **127**, 237201 (2021).
- [25] Rong Cong, Erick Garcia, Paola C. Forino, Anna Tasseti, Giuseppe Allodi, Arneil P. Reyes, Phoung M. Tran, Patrick M. Woodward, Cesare Franchini, Samuele Sanna, and Vesna F. Mitrović, “Effects of charge doping on Mott insulator with strong spin-orbit coupling, $\text{Ba}_2\text{Na}_{1-x}\text{Ca}_x\text{OsO}_6$,” *Phys. Rev. Mater.* **7**, 084409 (2023).
- [26] Sreekar Voleti, Koushik Pradhan, Subhro Bhattacharjee, Tanusri Saha-Dasgupta, and Arun Paramekanti, “Probing octupolar hidden order via janus impurities,” *npj Quantum Materials* **8**, 42 (2023).
- [27] Lorenzo Celiberti, Dario Fiore Mosca, Giuseppe Allodi, Leonid V. Pourovskii, Anna Tasseti, Paola Caterina Forino, Rong Cong, Erick Garcia, Phoung M. Tran, Roberto De Renzi, Patrick M. Woodward, Vesna F. Mitrović, Samuele Sanna, and Cesare Franchini, “Spin-orbital Jahn-Teller bipolarons,” *Nature Communications* **15**, 2429 (2024).
- [28] Cesare Franchini, Michele Reticcioli, Martin Setvin, and Ulrike Diebold, “Polarons in materials,” *Nature Reviews Materials* **6**, 560–586 (2021).
- [29] L. V. Pourovskii, “Two-site fluctuations and multipolar intersite exchange interactions in strongly correlated systems,” *Phys. Rev. B* **94**, 115117 (2016).
- [30] P Blaha, K Schwarz, G Madsen, D Kvasnicka, J Luitz, R Laskowski, F Tran, and L D Marks, *WIEN2k, An augmented Plane Wave + Local Orbitals Program for Calculating Crystal Properties* (Karlheinz Schwarz, Techn. Universität Wien, Austria, ISBN 3-9501031-1-2, 2018).
- [31] A. Georges, G. Kotliar, W. Krauth, and M. J. Rozenberg, “Dynamical mean-field theory of strongly correlated fermion systems and the limit of infinite dimensions,” *Rev. Mod. Phys.* **68**, 13–125 (1996).
- [32] V I Anisimov, A I Poteryaev, M A Korotin, A O Anokhin, and G Kotliar, “First-principles calculations of the electronic structure and spectra of strongly correlated systems: dynamical mean-field theory,” *Journal of Physics: Condensed Matter* **9**, 7359 (1997).
- [33] A. I. Lichtenstein and M. I. Katsnelson, “Ab initio calculations of quasiparticle band structure in correlated systems: LDA++ approach,” *Phys. Rev. B* **57**, 6884–6895 (1998).
- [34] M. Aichhorn, L. V. Pourovskii, P. Seth, V. Vildosola, M. Zingl, O. E. Peil, X. Deng, J. Mravlje, G. J. Kraberger, C. Martins, *et al.*, “TRIQS/DFTTools: A TRIQS application for ab initio calculations of correlated materials,” *Computer Physics Communications* **204**, 200–208 (2016).
- [35] J. Hubbard, “Electron correlations in narrow energy bands,” *Proc. Roy. Soc. (London)* **A 276**, 238 (1963).
- [36] L. V. Pourovskii and D. Fiore Mosca, “MagInt,” <https://github.com/MagInteract/MagInt>.
- [37] Supplementary Material.
- [38] Dario Fiore Mosca, Hermann Schnait, Lorenzo Celiberti, Markus Aichhorn, and Cesare Franchini, “The Mott transition in the $5d^1$ compound $\text{Ba}_2\text{NaOsO}_6$: A DFT+DMFT study with PAW spinor projectors,” *Computational Materials Science* **233**, 112764 (2024).
- [39] G. Chen, R. Pereira, and L Balents, “Exotic phases induced by strong spin-orbit coupling in ordered double perovskites,” *Phys. Rev. B* **82**, 174440 (2010).
- [40] C. Svoboda, W. Zhang, M. Randeria, and N. Trivedi, “Orbital order drives magnetic order in $5d^1$ and $5d^2$ double perovskite Mott insulators,” *Phys. Rev. B* **104**, 024437 (2021).
- [41] G. Chen and L Balents, “Spin-orbit coupling in d^2 ordered double perovskites,” *Phys. Rev. B* **84**, 094420 (2011).
- [42] Ahmed Rayyan, Xiaoyu Liu, and Hae-Young Kee, “Fate of multipolar physics in $5d^2$ double perovskites,” *Phys. Rev. B* **108**, 045149 (2023).
- [43] M Rotter, “Using mcphase to calculate magnetic phase diagrams of rare earth compounds,” *Journal of Magnetism and Magnetic Materials* **272-276**, E481–E482 (2004), proceedings of the International Conference on Magnetism (ICM 2003).
- [44] G. Kresse and J. Furthmüller, “Efficient iterative schemes for ab initio total-energy calculations using a plane-wave basis set,” *Phys. Rev. B* **54**, 11169–11186 (1996).
- [45] Dario Fiore Mosca, Leonid V. Pourovskii, and Cesare Franchini, “Modeling magnetic multipolar phases in density functional theory,” *Phys. Rev. B* **106**, 035127 (2022).

END MATTER

From t_{2g} - to J_{eff} - Hamiltonian

The t_{2g} -Hamiltonian of Eq.2 is defined in the spin+orbital many-electron basis states $|\tilde{\Gamma}(i)\rangle$, which, for the two-electron case, belong to the Hund's rule GS multiplet with the degeneracy $(2l+1)(2S+1) = 9$ for $S = 1$ and $l = 1$. The corresponding intersite exchange interactions (t_{2g} -IEI) can be downfolded onto the J_{eff} many-electron basis $|\Gamma(i)\rangle$. Here i is the magnetic site index (1 for d^1 and 2 for d^2 for simplicity). To this end, we introduce the projector operator $P_{LS}(i) = |\Gamma(i)\rangle\langle\tilde{\Gamma}(i)|$, such that any many-electron t_{2g} -shell operator $\tau_{s,l}^{\alpha,\beta}$ can be J_{eff} -projected as

$$\tilde{O}_{s,l}^{\alpha,\beta}(i) = P_{LS}(i) \tau_{s,l}^{\alpha,\beta}(i) P_{LS}^\dagger(i). \quad (3)$$

The multipole many-electron operators O_K^Q are expanded in terms of the projected operators through coefficients $c_{s\alpha,l\beta}^{KQ}(i) = \text{Tr}[\tilde{O}_{s,l}^{\alpha,\beta}(i)O_K^Q]$. Specifically, for the $(K, Q) = (3, -2)$ component, corresponding to the xyz octupole in Cartesian coordinates, this expansion yields the values listed in Tab. I for both d^1 and d^2 configurations.

The J_{eff} -IEI are then obtained by contracting these coefficients with the original interaction matrix elements:

$$V_{KK'}^{QQ'}(ij) = \sum_{s,l} \sum_{\alpha,\beta} I_{ss',ll'}^{\alpha\alpha',\beta\beta'}(ij) c_{s\alpha,l\beta}^{KQ}(i) c_{s'\alpha',l'\beta'}^{K'Q'}(j). \quad (4)$$

The difference between the resulting SO-projected t_{2g} -IEI matrix and the initial J_{eff} -IEI is shown in Fig. 4. The SO-projected IEI reproduce the overall structure (See SM [37]), with excellent agreement in the dipole-dipole channels, while higher-order multipolar terms are systematically underestimated. For instance, the octupole-octupole coupling V^{xyz} is ~ -0.6 meV for the d^2 - d^2 bond, compared to the expected -1.6 meV. This discrepancy likely originates from neglecting SO coupling in the excited d^1 and d^3 configurations in the superexchange processes, though further investigation is required.

SE operator		$c_{s\alpha,l\beta}^{KQ}$	
s, α	l, β	d^1	d^2
1, x	2, yz	-0.5757	-0.3826
1, y	2, xz	-0.5757	-0.3826
1, z	2, xy	0.5757	0.3826

TABLE I: Expansion coefficients for the octupolar operator O_3^{-2} in the spin+orbital basis.

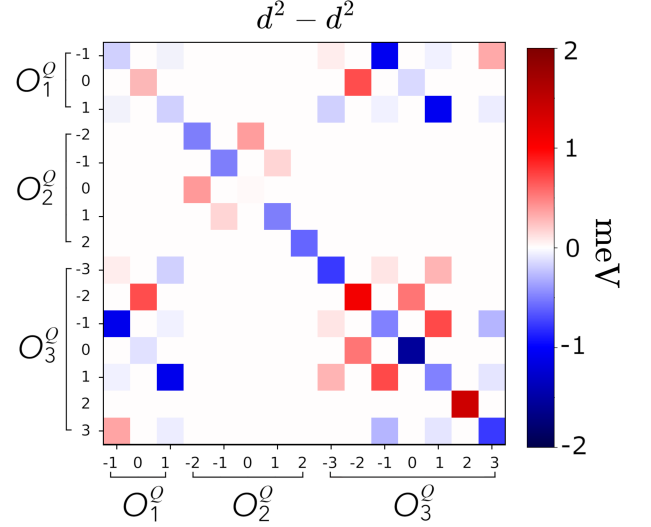


FIG. 4: Difference between the SO-projected t_{2g} -IEI and the IEI with DFT+SO for the $d^2 - d^2$ interaction bond $\mathbf{R}_{ij} = [0, 0.5, 0]$ in the supercell reference frame.

Origin of sign switch

As mentioned in the main text, we observe a reversal of the IEI already without SO coupling and within the t_{2g} -shell treatment. This is shown in Tab. II, where the t_{2g} -IEI are written, for the t_{2g} -shell operators leading to the V^{xyz} coupling.

To understand the origin of the sign switch, we compute the matrix elements of the d^1 one-electron t_{2g} -shell operator $\tau_{s,l}^{\alpha,\beta}(1)$ in the many-electron d^2 spin+orbital basis via

$$[T_{s,l}^{\alpha,\beta}(2)]_{MM'} = \langle\tilde{\Gamma}(2)M|\tau_{s,l}^{\alpha,\beta}(1)|\tilde{\Gamma}(2)M'\rangle. \quad (5)$$

We then express the resulting operator in terms of d^2 many-electron operators $\tau_{s',l'}^{\alpha',\beta'}(2)$ by fitting its components through $t_{ss',ll'}^{\alpha\alpha',\beta\beta'} = \text{Tr}[\tau_{s',l'}^{\alpha',\beta'}(2)T_{s,l}^{\alpha,\beta}(2)]$. In the expansion, we find the correct matrices of 2-electrons operators ($s = s', l = l', \alpha = \alpha', \beta = \beta'$), but with different signs for different components:

i) $t_{ss,ll}^{\alpha\alpha,\beta\beta} = -1$ for $(s, l) = (0, 2)$, i.e. for pure orbital-quadrupole terms.

ii) $t_{ss',ll'}^{\alpha\alpha,\beta\beta} = 1$ for both $(s, l) = (0, 1)$ dipole-orbital terms and $(s, l) = (1, 0)$ spin-dipole terms. The sign reversal thus arises in cases where multiplicative contributions remain uncompensated; for instance, when a spin-dipole coupled to an orbital-quadrupole on a d^2 site interacts with the corresponding spin-dipole orbital-quadrupole term on a d^1 site.

	$d^2 - d^2$			$d^1 - d^2$		
	$x; yz$	$y; xz$	$z; xy$	$x; yz$	$y; xz$	$z; xy$
$x; yz$	-2.62			2.97		
$y; xz$		-2.62			2.97	
$z; xy$			1.23			-1.39

TABLE II: t_{2g} -IEI couplings for $\tau_{s,l}$ with $(s,l) = (1,2)$, i.e. spin-dipole and orbital-quadrupole operators. The corresponding (α, β) components are listed. These couplings project onto the spin-orbit V^{xyz} octupole-octupole intersite exchange. Values are reported for $\mathbf{R}_{ij} = [0, 0.5, 0]$ in the supercell reference frame of Fig. 2a.

Mean Field analysis of T_o

A detailed analysis of the evolution of T_o with Na concentration is necessary. As discussed in the main text, the V^{xyz} octupolar interaction changes only weakly between $x = 0$ and $x = 0.125$. Yet the ordering temperature decreases noticeably, especially at higher doping levels ($x = 0.25$) in the undistorted cubic structure. Interestingly, at these Na concentrations, despite the sign change in the IEI, the system remains non-frustrated: reversing both the interactions and the order parameters leaves the total energy unchanged.

To isolate the microscopic origin of the lowering of T_o upon Na doping, we performed a *gedankenexperiment* in which we fixed IEI for the FO ordered pristine case ($\delta = 0$), while varying the rcf and pcf splittings incrementally (See Figure 5a,b). The results show a strong dependence of T_o on the rcf, saturating at ~ 45 meV to ≈ 112 K and decreasing to roughly half the value when the rcf is reduced to ~ 6 meV. Any lower rcf makes the T_{2g} levels magnetically active and promotes dipolar order. In contrast, the pcf exerts only a weak, nearly linear influence: increasing it up to 6 meV lowers T_o by only a few percent. Higher values were not explored, as stronger pcf terms would induce significant T_{2g} mixing in the E_g doublet and alter the qualitative physics.

While variations in the rcf and pcf account for part of the observed suppression of T_o , they do not capture the full picture. An additional factor is the difference in the total angular momentum GSMs between the d^2 ($J_{\text{eff}} = 2$) and d^1 ($J_{\text{eff}} = 3/2$) configurations. Indeed, as seen in Fig. 5a, even for rcf values of ~ 20 meV, the $J_{\text{eff}} = 2$ GSM does not yet fully project onto a pseudospin-1/2 subspace, with clear implications in the ordering behavior.

To assess the effect of GSM mismatch, we performed a second *gedankenexperiment* in which all intersite exchange interactions except the octupole-octupole V^{xyz} were set to zero. The doping concentration was then varied by progressively substituting d^2 sites with d^1 ones,

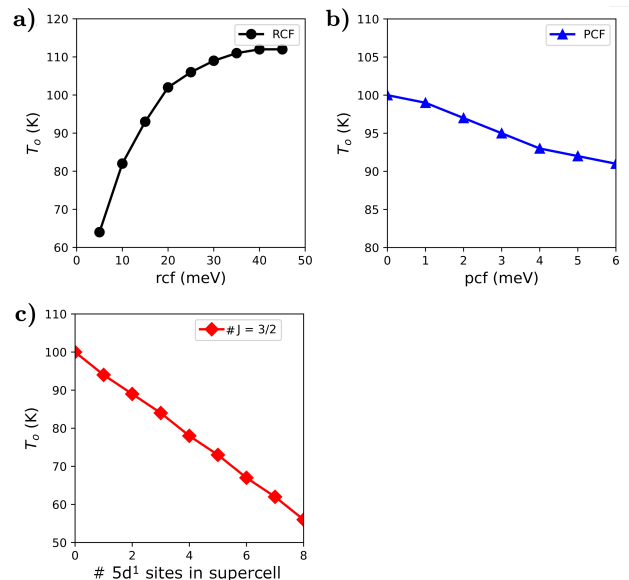


FIG. 5: Mean-field ordering temperature T_o as a function of (a) remnant crystal field (rcf) within the $J_{\text{eff}} = 2$ ground-state multiplet (GSM), and (b) polaron crystal field (pcf) for the IEI computed in the full d^2 BCOO compound. (c) T_o as a function of the number of hole-polarons ($J_{\text{eff}} = 3/2$ GSMs) in the supercell with only the V^{xyz} octupole-octupole IEI active.

effectively replacing the $J_{\text{eff}} = 2$ GSM (with its ~ 20 meV rcf) by the $J_{\text{eff}} = 3/2$ GSM (Fig. 5c). This procedure preserves the stability of the FO solution across all doping levels and isolates the role of the GSMs. The resulting T_o decreases linearly with increasing d^1 concentration, again in agreement with the trend observed both in our calculations and in experimental observations.

Additional mechanisms, such as static or dynamic Jahn-Teller effects on the d^1 polarons, or d^1 - d^1 quadrupole-quadrupole dimerization and dopant-induced strains may also affect the ordering temperature, but their investigation is beyond the scope of the present work.

Supplementary material for 'Polaron-driven switching of octupolar order in doped 5d² double perovskite'

Dario Fiore Mosca,^{1,2,3} Lorenzo Celiberti,¹ Leonid V. Pourovskii,^{2,3} and Cesare Franchini^{1,4}

¹*University of Vienna, Faculty of Physics, Center for Computational Materials Science, Kolingasse 14-16, 1090, Vienna, Austria*

²*CPHT, CNRS, École polytechnique, Institut Polytechnique de Paris, 91120 Palaiseau, France*

³*Collège de France, Université PSL, 11 place Marcelin Berthelot, 75005 Paris, France*

⁴*Department of Physics and Astronomy "Augusto Righi", Alma Mater Studiorum - Università di Bologna, Bologna, 40127 Italy*

(Dated: March 20, 2026)

I. FIRST PRINCIPLES METHODS

In the following, we describe our first principles calculations. In A. we detail the electronic structure calculation of paramagnetic Ba₂Ca_{1- δ} Na _{δ} OsO₆ with both virtual approximation and chemical substitution, in B. the calculation of Intersite Exchange Interactions (IEI) for both the spin-orbit J_{eff} ground state multiplets (GSMs) and (s, l) spin+orbital t_{2g} -shell. In C. we detail the modeling of octupolar polaron in constrained density functional theory (DFT) + U.

A. Correlated electronic structure calculations

We calculate the paramagnetic electronic structure of Ba₂Ca_{1- δ} Na _{δ} OsO₆ using the charge self-consistent DFT¹ + dynamical mean-field theory (DMFT)²⁻⁵ within the quasi-atomic Hubbard-I (HI) approximation⁶ based on the full-potential LAPW code Wien2k¹, incorporating spin-orbit (SO) coupling via the standard variational treatment.

To model doping we utilize an 8 f.u. supercell obtained from the cubic Ba₂CaOsO₆ structure, with lattice parameters $\sqrt{2}a \times \sqrt{2}a \times a$ and $a = 8.346 \text{ \AA}$ ⁷. Doping concentration $\delta = 0.125$ is obtained using the virtual crystal approximation, achievable by reducing the total electron count by one. Additional calculations incorporating explicit chemical doping, as presented in Sec. IV, have been done by explicitly substituting the Ca ion at position [0, 0, 0.5] by one Na.

We employ the local density approximation (LDA) for the DFT exchange-correlation potential, a 30 \mathbf{k} -point mesh across the full Brillouin zone and a basis cutoff of $R_{\text{mt}}K_{\text{max}} = 7$. For the correlated space projection, we consider the Wannier orbitals representing the full Os d states constructed from the manifold of Kohn-Sham bands within the energy window [-1.36 : 5.44] eV relative to the Fermi level.

The polaronic 5d¹ localization in DFT+HI is enforced via the double-counting correction in the fully localized limit by explicitly setting the d^1 electron count on the polaronic site, while nominal d^2 are maintained for all other Os sites. For the DFT+HI calculation, we employ the d -shell parameters $F^0 = U = 3.2 \text{ eV}$ and $J_H = 0.5 \text{ eV}$ on all sites, consistent with previous studies on d^1 and d^2 DPS^{8,9}.

B. Calculation J_{eff} -IEI and t_{2g} -IEI

The multipolar IEI of both Eq. 1 (Main) and Eq. 2 (Main) are determined using the Force-Theorem in HI (FT-HI) method described in Ref¹⁰. This approach involves inducing small symmetry-breaking fluctuations in the density matrix of the GSMs occurring simultaneously at two neighboring magnetic (Os) sites, i and j . The interaction terms $V_{QQ'}^{KK'}(ij)/I_{ss',ll'}^{\alpha\alpha',\beta\beta'}$ are then extracted by analyzing how the DFT+DMFT grand potential responds to these two-site fluctuations. Detailed explanations can be found in the Appendix of Ref.¹¹ and the Supplementary Material of Ref.⁸, with the full derivation provided in Ref.¹⁰. The reference frame for the calculated IEI is aligned with the local octahedral axes shown in Figure 2b (Main), which are rotated 45° relative to the cubic crystallographic [100] axis. When necessary, like for physical magnetic moments in the global crystallographic frame, a further 45° rotation is applied.

C. Modeling of octupolar polaron in DFT + U

The polaronic localization is obtained at DFT+U level by adopting the constrained initialization of the on-site density matrix (ODM) as introduced in Ref.¹². This method constructs an ODM for each site based on the order parameters

of the FO and $\text{AF}\mathcal{O}$ polaronic multipolar phases. In the J_{eff} space, the ODM is expressed as:

$$\rho_{HI}^{mm'} = \text{Tr}[\rho_{MM'}^{mm'}(J_{\text{eff}})\hat{\rho}_{\alpha}(J_{\text{eff}})] \quad (1)$$

where $\rho_{MM'}^{mm'}(J_{\text{eff}})$ is the matrix element of the ODM operator in the GSM basis and $\hat{\rho}_{\alpha}(J_{\text{eff}})$ is the many-electron density matrix derived from the GSM for a given phase. For instance, to initialize the octupolar polaron configuration, we define $\hat{\rho}_{\alpha} = \hat{O}_{xyz}c_{xyz}$ for all d^2 sites and $\hat{\rho}_{\alpha} = -\hat{O}_{xyz}c_{xyz}$ for the polaronic d^1 site, where $c_{xyz} \equiv \langle \hat{O}_{xyz} \rangle$ is the expectation value of the xyz octupole at site α .

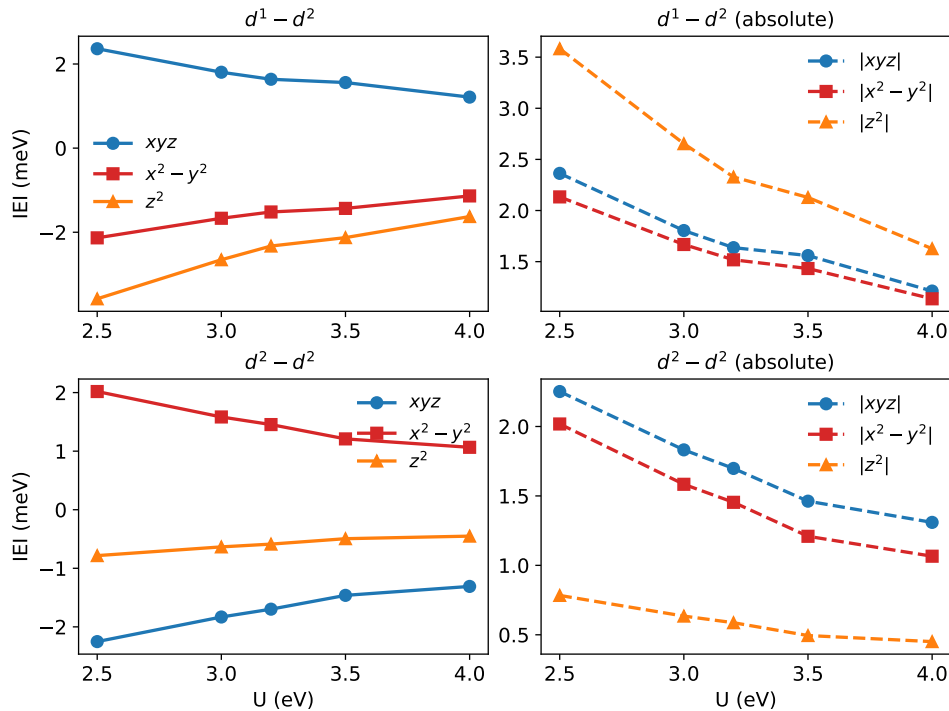
The many electron DM $\hat{\rho}_{\alpha}(J_{\text{eff}})$ contains, by construction, the nominal number of correlated electrons included in the effective low-energy Hamiltonian. Before the DFT+U self-consistent cycle, this number is corrected to account for the strong hybridization effects that enhance $5d$ orbital occupations in double perovskites^{12,13}. We find the total electron number in our DFT+U ODMs to be ≈ 5.95 and ≈ 5.93 for d^2 and d^1 sites respectively. Further details of this procedure can be found in Ref.¹². The initialized ODMs can be found in Sec. V.

The DFT+U calculations were performed using the Vienna Ab Initio Simulation Package (VASP)^{14,15}, employing the Perdew-Burke-Ernzerhof (PBE) generalized gradient approximation. The on-site Coulomb repulsion at the Os d orbitals was applied using the rotationally-invariant Lichtenstein formulation of DFT+U¹⁶. We used the on-site Coulomb $U = 3.2$ eV and $J_H = 0.5$ eV, consistent with prior studies^{9,12}. The reciprocal space was sampled with a k-point spaced mesh of 0.1 \AA^{-1} , the plane wave energy cutoff of 550 eV was used together with an energy convergence of 10^{-4} eV. The structural relaxation was performed using the Blocked-Davidson algorithm, allowing for the optimization of cell volume, cell shape, and atomic positions with a convergence accuracy of 10^{-2} \AA/eV on the atomic forces.

II. STABILITY OF IEI AND METHODOLOGICAL CONSIDERATIONS

We have investigated the dependence of the IEI on the Hubbard interaction U by performing a series of calculations in which U is varied from 2.5 to 4.0 eV in steps of 0.5 eV. Figure 1 shows the resulting evolution of the octupole–octupole (V^{xyz}) and quadrupole–quadrupole ($V^{x^2-y^2}$, V^{z^2}) IEI for the $\mathbf{R} = [0, 0.5, 0]$ bond in the supercell reference frame, for both $d^1 - d^2$ and $d^2 - d^2$ pairs.

Across the entire range of U values considered, the qualitative behavior of the exchange interactions remains unchanged. In particular, the octupole–octupole interaction V^{xyz} on the d^2 sites remains the dominant contribution and its sign and relative strength are preserved. Consequently, the switching of the octupolar order induced by the presence of polarons, the main result of this work, is robust with respect to variations of U . Changes in U within the physically relevant range do not modify the underlying multipolar ordering tendencies on either the d^2 or the d^1 sublattices.



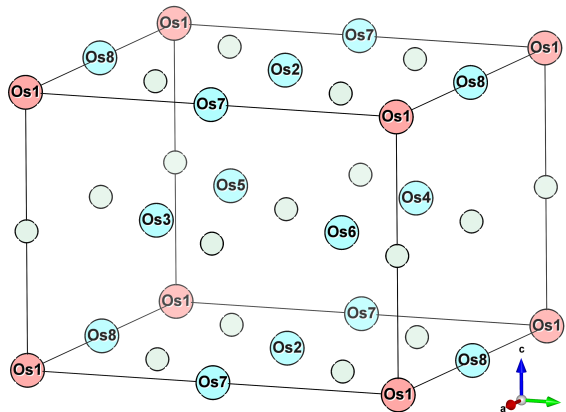
Supplementary Figure 1: V^{xyz} (xyz), $V^{x^2-y^2}$ ($x^2 - y^2$) and V^{z^2} (z^2) IEI as a function of U for the $\mathbf{R} = [0, 0.5, 0]$ bond in the supercell reference frame for (a) $d^1 - d^2$ and (c) $d^2 - d^2$ interactions, and (b, d) the respective absolute values.

Recently, symmetry-breaking approaches such as special quasirandom structure (SQS) models have been proposed to capture insulating behavior¹⁷ and have been applied, among other systems, to heavy transition-metal oxides^{18,19}. Osmium double perovskites, however, present a particular challenge for this approach. Their magnetically ordered phase is characterized by multipolar order, in which conventional magnetic dipole moments are absent, complicating the definition of a physically meaningful paramagnetic reference state. Moreover, studies of $5d^1$ osmium double perovskites have shown that simulations based on randomly disordered local spin orientations require an explicit on-site Hubbard- U correction to open an insulating gap^{20,21}. This indicates that these systems cannot be regarded as genuine local-moment paramagnetic insulators. Instead, their insulating behavior appears to emerge from a nontrivial interplay of electronic correlations, spin–orbit coupling, and lattice-symmetry breaking; a scenario that warrants further investigation.

III. DOPING CONCENTRATION $\delta = 0.125$ WITH VIRTUAL CRYSTAL APPROXIMATION

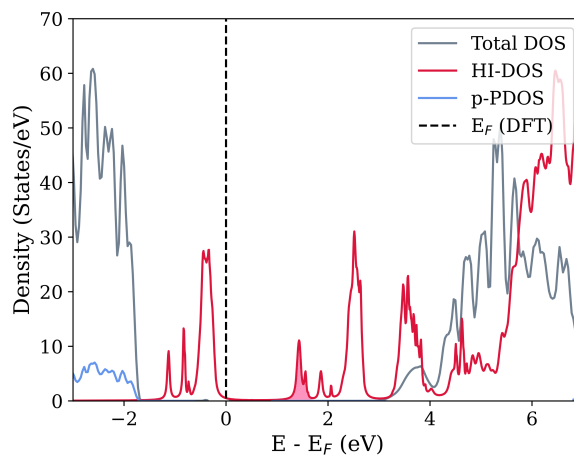
In the following, we present DFT+HI, FT-HI, and mean-field (MF) results for $\text{Ba}_2\text{Ca}_{1-\delta}\text{Na}_\delta\text{OsO}_6$ within the virtual crystal approximation at Na doping concentration $\delta = 0.125$. Section A describes the structural details, Section B reports the DFT+HI Density of States (DOS), Section C discusses the J_{eff} -IEI, Section D analyzes the crystal-field splittings and ground-state multiplet wavefunctions, and Section E presents the ordered phase and the MF order parameters as a function of temperature. Lastly, Section F presents the spin+orbital t_{2g} -IEI.

A. Structure



Supplementary Figure 2: Supercell of $\text{Ba}_2\text{Ca}_{1-\delta}\text{Na}_\delta\text{OsO}_6$ with labels for the osmium ions as indexed in the next Sections. The polaron is localized on the Os1 (light red).

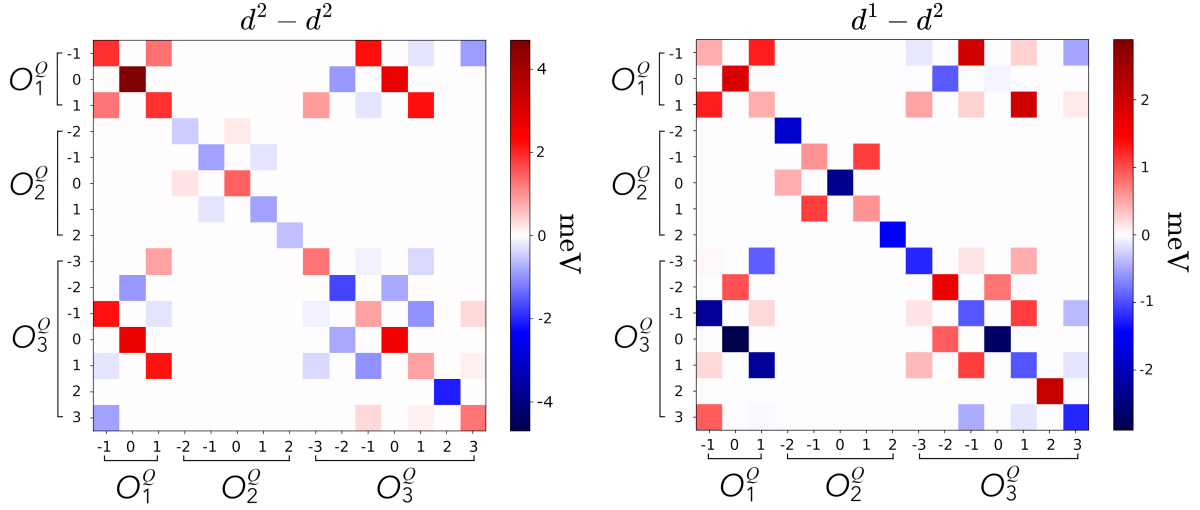
B. Polaronic density of States in DFT, DFT+HI



Supplementary Figure 3: Combined the DFT and DFT+HI DOS. The hole-polaron peak is highlighted in light-red.

C. Intersite Exchange Interactions in J_{eff} basis

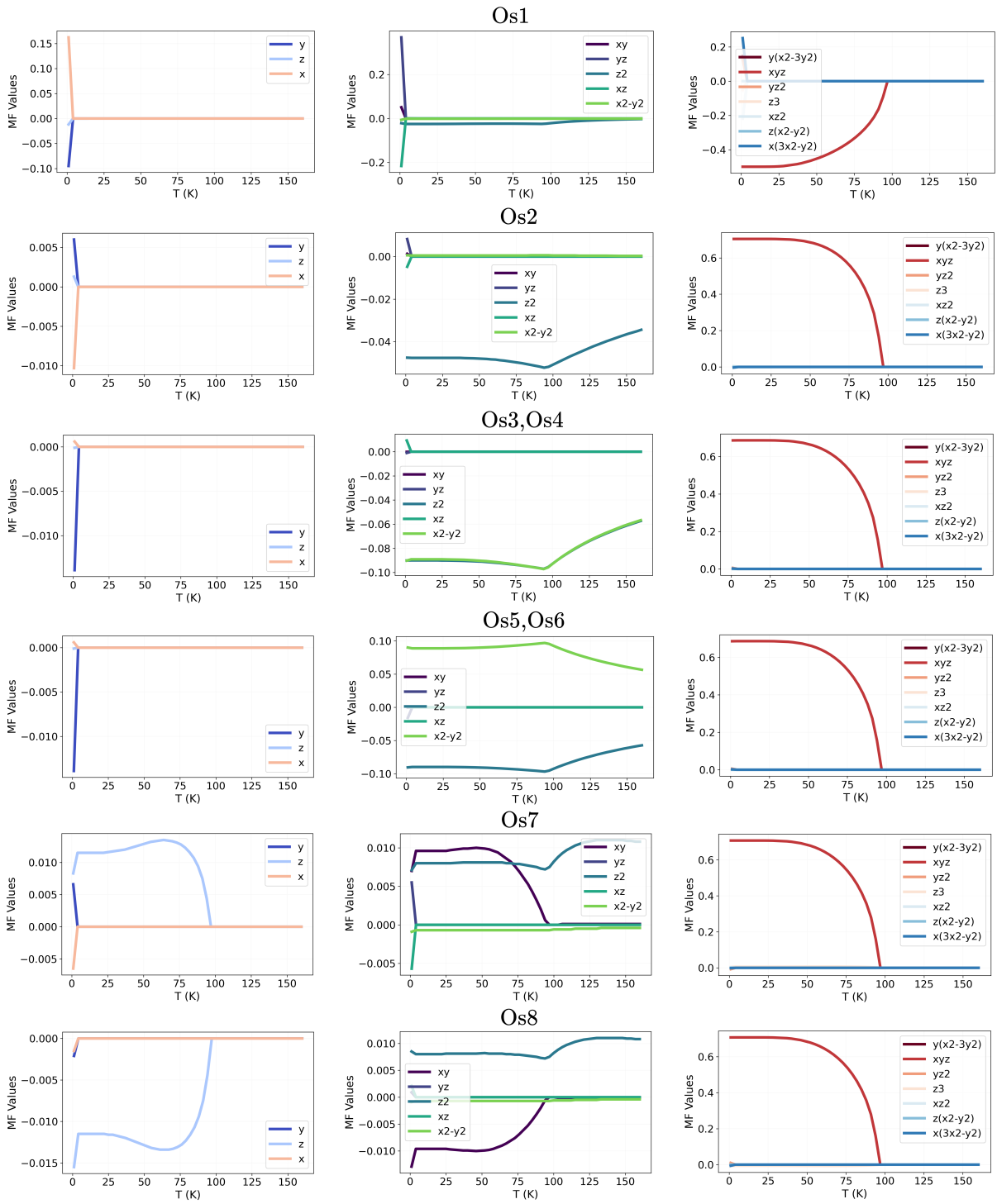
In Suppl. Fig. 4, the IEI in $\text{Ba}_2\text{Ca}_{1-\delta}\text{Na}_\delta\text{OsO}_6$ are shown as a color map, with the corresponding values listed in Suppl. Table II for the two cases of d^2-d^2 and d^1-d^2 electronic configurations. For the d^1-d^2 bond, both quadrupole-quadrupole and dipole-octupole interactions acquire antisymmetric components due to the inversion-symmetry breaking introduced by the polaron. The role of these antisymmetric interactions remains an open question and deserves further investigation.



Supplementary Figure 4: Color map of the IEI $V_{KK'}^{QQ'}$ in $\text{Ba}_2\text{Ca}_{1-\delta}\text{Na}_\delta\text{OsO}_6$ at pressure $[0,1/2,0]$ Os-Os pair for (left) $d^2 - d^2$ interaction and (right) $d^1 - d^2$ interaction. All values are in meV. The numerical list of $V_{KK'}^{QQ'}$ is given in Suppl. Table II.

Supplementary Table I: Calculated IEI $V_{KK'}^{QQ'}$ for the $J_{\text{eff}} = 3/2/J_{\text{eff}} = 2$ multiplets. The first two columns list Q and Q' , while the third and fourth columns display the KQ and $K'Q'$ tensors in Cartesian representation. The last three columns report the IEI values (in meV) for the $[0, 1/2, 0]$ nearest-neighbor Os–Os bond in the supercell reference frame, comparing: (i) d^2 – d^2 interactions from Ref.⁹, (ii) d^2 – d^2 interactions from this work, and (iii) d^1 – d^2 interactions from this work. A slash denotes the reversed Q/Q' case, highlighting the asymmetric contributions.

Bonds $\mathbf{R}_{ij} = [0.5, 0.5, 0]$ (primitive cell)				$d^2 - d^2$ (Ref. ⁹)	$d^2 - d^2$	$d^1 - d^2$
Dipole-Dipole						
-1	-1	y	y	1.62	1.89	0.45
0	0	z	z	4.17	4.70	1.87
1	-1	x	y	1.26	1.28	1.28
1	1	x	x	1.62	1.89	0.45
Quadrupole-Quadrupole						
-2	-2	xy	xy	-0.41	-0.45	-1.84
-1	-1	yz	yz	-0.79	-0.85	0.59
0	-2	z^2	xy	0.16	0.22	0.47/-0.01
0	0	z^2	z^2	1.32	1.45	-2.33
1	-1	xz	yz	-0.23	-0.24	1.09
1	1	xz	xz	-0.79	-0.85	0.59
2	2	x^2-y^2	x^2-y^2	-0.58	-0.59	-1.52
Octupole-Octupole						
-3	-3	$y(x^2-3y^2)$	$y(x^2-3y^2)$	1.16	1.26	-1.24
-2	-2	xyz	xyz	-1.49	-1.70	1.64
-1	-3	yz^2	$y(x^2-3y^2)$	-0.14	-0.13	0.16
-1	-1	yz^2	yz^2	0.80	0.87	-0.95
0	-2	z^3	xyz	-0.79	-0.80	0.78
0	0	z^3	z^3	2.35	2.58	-2.69
1	-3	xz^2	$y(x^2-3y^2)$	-0.29	-0.35	0.39/0.46
1	-1	xz^2	yz^2	-0.98	-0.76	1.11
1	1	xz^2	xz^2	0.80	0.86	-0.95
2	2	$z(x^2-y^2)$	$z(x^2-y^2)$	-1.89	-2.08	2.09
3	-1	$x(3x^2-y^2)$	yz^2	0.29	0.35	-0.39
3	1	$x(3x^2-y^2)$	xz^2	0.14	0.12	-0.15
3	3	$x(3x^2-y^2)$	$x(3x^2-y^2)$	1.16	1.26	-1.24
Dipole-Octupole						
-1	-3	y	$y(x^2-3y^2)$		-0.01	-0.13/0.04
-1	-1	y	yz^2	1.97	2.21	1.97/-2.27
-1	1	y	xz^2	-0.20	-0.23	0.26/0.21
-1	3	y	$x(3x^2-y^2)$	-0.89	-0.89	-0.51/0.91
0	-2	z	xyz	-0.97	-0.95	-0.95/0.98
0	0	z	z^3	2.38	2.74	-0.07/-2.89
0	2	z	$z(x^2-3y^2)$		0.01	
1	-3	x	$y(x^2-3y^2)$	0.89	0.88	0.51/-0.91
1	-1	x	yz^2	-0.20	-0.23	0.26/0.21
1	1	x	xz^2	1.97	2.21	1.98/-2.27
1	3	x	$x(3x^2-y^2)$		0.01	0.13/-0.04



Supplementary Figure 5: MF values of multipolar operators O_K^Q expressed in Cartesian coordinates as a function of temperature for the different osmium ions of Fig. 2.

F. Intersite Exchange Interactions in spin+orbital t_{2g} basis

In the following, the non-SOC t_{2g} -IEI of $\text{Ba}_2\text{Ca}_{1-\delta}\text{Na}_\delta\text{OsO}_6$ in the spin+orbital basis are listed. The t_{2g} -IEI refer to the $I_{ss',ll'}^{\alpha\alpha',\beta\beta'}(ij)$ of equation (2) in the main.

Supplementary Table II: Calculated IEI $I_{ss',ll'}^{\alpha\alpha',\beta\beta'}(ij)$ for the spin+orbital t_{2g} basis. The first two columns list spin- s component (α) and orbital- l component β on the first site, while the other two list spin- s' component (α') and orbital- l' component β' of the second site. The last two columns report the IEI values (in meV) for the $[0, 1/2, 0]$ nearest-neighbor Os–Os bond in the supercell reference frame, comparing: (i) d^2 – d^2 interactions and (ii) d^1 – d^2 interactions. The values highlighted in bold are the ones who map onto xyz J_{eff} -IEI.

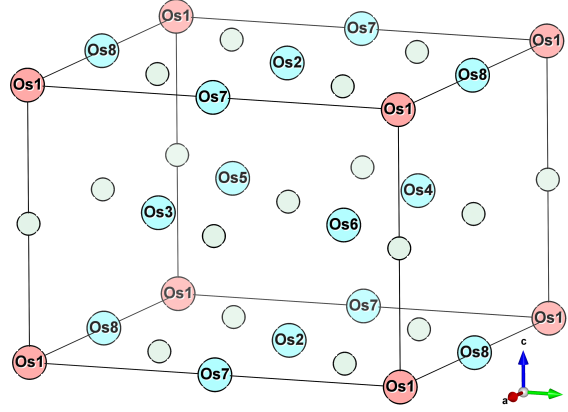
Bonds $\mathbf{R}_{ij} = [0.5, 0.5, 0]$ (primitive cell)				$d^2 - d^2$	$d^1 - d^2$
$(s; l) - (s'; l')$					
(Monopole;Dipole)-(Monopole;Dipole)					
1	y	1	y	-4.42	-4.24
1	y	1	x	2.78	2.92
1	z	1	z	0.92	0.76
1	x	1	x	-4.42	-4.24
(Monopole;Dipole)-(Monopole;Quadrupole)					
1	y	1	xy	-0.04	-0.06
1	y	1	z^2	0.03	-0.04
1	x	1	xy	0.04	0.06
1	x	1	z^2	-0.03	0.04
(Monopole;Quadrupole)-(Monopole;Quadrupole)					
1	xy	1	xy	2.31	-2.21
1	xy	1	z^2	0.87	-1.39
1	yz	1	yz	-4.72	4.55
1	yz	1	xz	-3.03	3.19
1	z^2	1	z^2	10.07	-10.05
1	xz	1	xz	-4.72	4.55
1	x^2-y^2	1	x^2-y^2	0.97	-0.78
(Dipole;Monopole)-(Dipole;Monopole)					
y	1	y	1	10.83	5.75
z	1	z	1	10.83	5.75
x	1	x	1	10.83	5.75
(Dipole;Monopole)-(Dipole;Dipole)					
y	1	y	y	-0.11	0.04
y	1	y	x	0.11	-0.04
z	1	z	y	-0.11	0.04
z	1	z	x	0.11	-0.04
x	1	x	y	-0.11	0.04
x	1	x	x	0.11	-0.04
(Dipole;Monopole)-(Dipole;Quadrupole)					
y	1	y	xy	-1.85	-0.93
y	1	y	z^2	5.65	2.87
z	1	z	xy	-1.85	-0.93
z	1	z	z^2	5.65	2.87
x	1	x	xy	-1.85	-0.93
x	1	x	z^2	5.65	2.87

Bonds $\mathbf{R}_{ij} = [0.5, 0.5, 0]$ (primitive cell)				$d^2 - d^2$	$d^1 - d^2$
$(s; l) - (s'; l')$					
(Dipole;Dipole)-(Dipole;Dipole)					
y	y	y	y	-2.82	-3.24
y	y	y	x	1.74	2.18
y	z	y	z	0.60	0.60
y	x	y	x	-2.82	-3.24
z	y	z	y	-2.82	-3.24
z	y	z	x	1.74	2.18
z	z	z	z	0.60	0.60
z	x	z	x	-2.82	-3.24
x	y	x	y	-2.82	-3.24
x	y	x	x	1.74	2.18
x	z	x	z	0.60	0.60
x	x	x	x	-2.82	-3.24
(Dipole;Dipole)-(Dipole;Quadrupole)					
y	y	y	xy	-0.03	-0.05
y	x	y	xy	0.02	0.05
z	y	z	xy	-0.03	-0.05
z	x	z	xy	0.02	0.05
x	y	x	xy	-0.03	-0.05
x	x	x	xy	0.02	0.05
(Dipole;Quadrupole)-(Dipole;Quadrupole)					
y	xy	y	xy	1.23	-1.39
y	xy	y	z^2	0.39	-0.78
y	yz	y	yz	-2.62	2.98
y	yz	y	xz	-1.59	1.96
y	z^2	y	z^2	5.58	-6.53
y	xz	y	xz	-2.62	2.98
y	x^2-y^2	y	x^2-y^2	0.57	-0.56
z	xy	z	xy	1.23	-1.39
z	xy	z	z^2	0.39	-0.78
z	yz	z	yz	-2.62	2.98
z	yz	z	xz	-1.59	1.96
z	z^2	z	z^2	5.58	-6.53
z	xz	z	xz	-2.62	2.98
z	x^2-y^2	z	x^2-y^2	0.57	-0.56
x	xy	x	xy	1.23	-1.39
x	xy	x	z^2	0.39	-0.78
x	yz	x	yz	-2.62	2.98
x	yz	x	xz	-1.59	1.96
x	z^2	x	z^2	5.58	-6.53
x	xz	x	xz	-2.62	2.98
x	x^2-y^2	x	x^2-y^2	0.57	-0.56

IV. DOPING CONCENTRATION $\delta = 0.125$ FROM CONSTRAINED DFT+U STRUCTURE

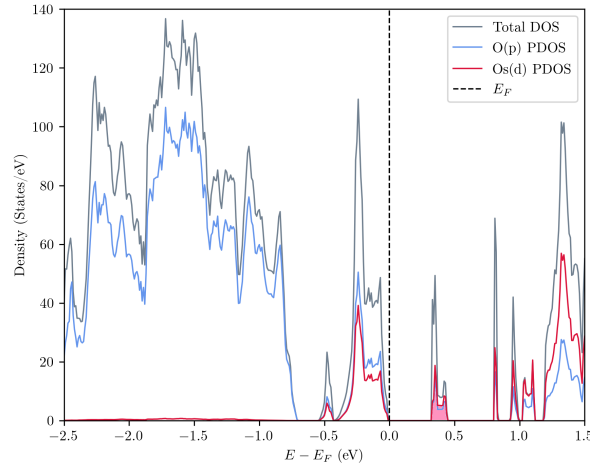
In the following, we present DFT+HI, FT-HI, and mean-field (MF) results for $\text{Ba}_2\text{Ca}_{1-\delta}\text{Na}_\delta\text{OsO}_6$ within the virtual crystal approximation at Na doping concentration $\delta = 0.125$ and with the polaronic distorted structure obtained from constrained DFT+U calculation. Section A describes the structural details, Section B reports the DFT+HI density of states, Section C discusses the J_{eff} -IEI, Section D analyzes the crystal-field splittings and ground-state multiplet wavefunctions, and Section E presents the ordered phase and the MF order parameters as a function of temperature.

A. Structure



Supplementary Figure 6: Supercell of $\text{Ba}_2\text{Ca}_{1-\delta}\text{Na}_\delta\text{OsO}_6$ with labels for the osmium ions as indexed in the next Sections. The polaron is localized on the Os1 (light red).

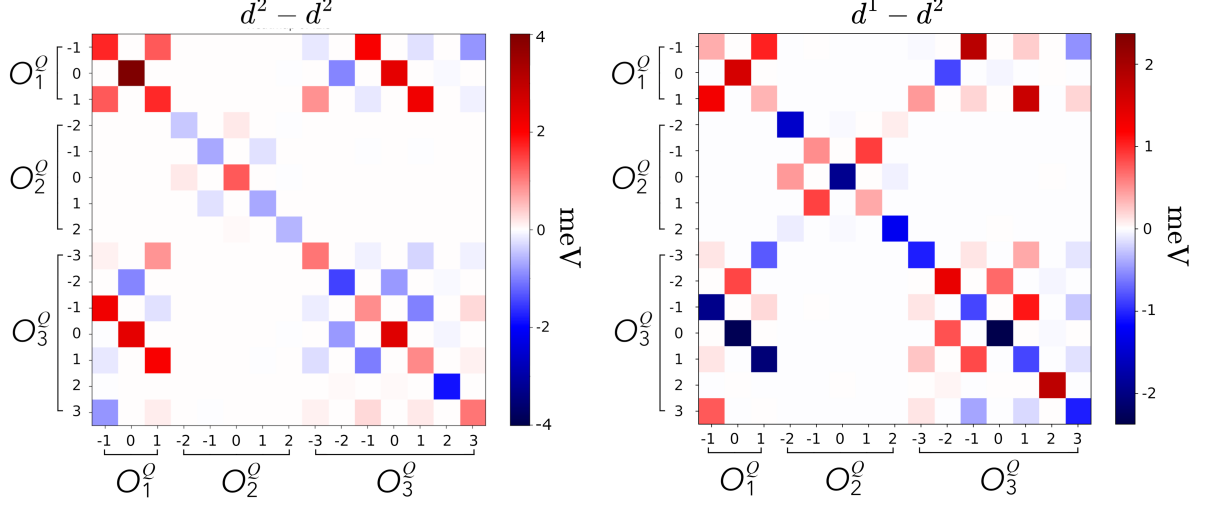
B. Polaronic density of States in constrained DFT+U



Supplementary Figure 7: DOS from constrained DFT+U. The hole-polaron peak is highlighted in light-red.

C. Intersite Exchange Interactions in J_{eff} basis

In Suppl. Fig. 8, the IEI in $\text{Ba}_2\text{Ca}_{1-\delta}\text{Na}_\delta\text{OsO}_6$ are shown as a color map, with the corresponding values listed in Suppl. Table III for the two cases of d^2-d^2 and d^1-d^2 electronic configurations. For the d^1-d^2 bond, an even stronger antisymmetric IEI matrix appears both in quadrupole-quadrupole and dipole-octupole interactions induced by the polaron.



Supplementary Figure 8: Color map of the IEI $V_{KK'}^{QQ'}$ in $\text{Ba}_2\text{Ca}_{1-\delta}\text{Na}_\delta\text{OsO}_6$ at pressure $[0,1/2,0]$ Os-Os pair for (left) $d^2 - d^2$ interaction and (right) $d^1 - d^2$ interaction. All values are in meV. The numerical list of $V_{KK'}^{QQ'}$ is given in Suppl. Table III.

Supplementary Table III: Calculated IEI $V_{KK'}^{QQ'}$ for the $J_{\text{eff}} = 3/2/J_{\text{eff}} = 2$ multiplets. The first two columns list Q and Q' , while the third and fourth columns display the KQ and $K'Q'$ tensors in Cartesian representation. The last three columns report the IEI values (in meV) for the $[0, 1/2, 0]$ nearest-neighbor Os–Os bond in the supercell reference frame, comparing: (i) d^2 – d^2 interactions from Ref.⁹, (ii) d^2 – d^2 interactions from this work, and (iii) d^1 – d^2 interactions from this work. A slash denotes the reversed Q/Q' case, highlighting the asymmetric contributions.

Bonds $\mathbf{R}_{ij} = [0.5, 0.5, 0]$ (primitive cell)				$d^2 - d^2$ (Ref. ⁹)	$d^2 - d^2$	$d^1 - d^2$
Dipole-Dipole						
-1	-1	y	y	1.62	1.70	0.39
0	0	z	z	4.17	4.01	1.56
1	-1	x	y	1.26	1.30	1.03
1	1	x	x	1.62	1.68	0.35
Quadrupole-Quadrupole						
-2	-2	xy	xy	-0.41	-0.42	-1.52
-2	2	xy	x^2-y^2			0.09/-0.09
-1	-1	yz	yz	-0.79	-0.69	0.53
0	-2	z^2	xy	0.16	0.17	0.48/-0.02
0	0	z^2	z^2	1.32	1.29	-1.92
1	-1	xz	yz	-0.23	-0.23	0.90
1	1	xz	xz	-0.79	-0.68	0.40
2	2	x^2-y^2	x^2-y^2	-0.58	-0.56	-1.27
Octupole-Octupole						
-3	-3	$y(x^2-3y^2)$	$y(x^2-3y^2)$	1.16	1.10	-1.05
-2	-2	xyz	xyz	-1.49	-1.46	1.39
-1	-3	yz^2	$y(x^2-3y^2)$	-0.14	-0.11	0.12
-1	-1	yz^2	yz^2	0.80	0.89	-0.86
0	-2	z^3	xyz	-0.79	-0.80	0.8/0.7
0	0	z^3	z^3	2.35	2.51	-2.37
1	-3	xz^2	$y(x^2-3y^2)$	-0.29	-0.31	0.27/0.40
1	-1	xz^2	yz^2	-0.98	-0.99	1.08
1	1	xz^2	xz^2	0.80	0.92	-0.87
2	2	$z(x^2-y^2)$	$z(x^2-y^2)$	-1.89	-1.87	1.78
3	-1	$x(3x^2-y^2)$	yz^2	0.29	0.30	-0.25
3	1	$x(3x^2-y^2)$	xz^2	0.14	0.12	-0.14
3	3	$x(3x^2-y^2)$	$x(3x^2-y^2)$	1.16	1.09	-1.05
Dipole-Octupole						
-1	-3	y	$y(x^2-3y^2)$		0.10	-0.03/0.12
-1	-1	y	yz^2	1.97	2.21	1.82/-1.96
-1	1	y	xz^2	-0.20	-0.16	0.26/0.12
-1	3	y	$x(3x^2-y^2)$	-0.89	-0.84	-0.51/0.77
0	-2	z	xyz	-0.97	-0.95	-0.85/0.87
0	0	z	z^3	2.38	2.41	-0.04/-2.31
0	2	z	$z(x^2-3y^2)$		0.03	0.01/0.01
1	-3	x	$y(x^2-3y^2)$	0.89	0.82	0.47/-0.77
1	-1	x	yz^2	-0.20	-0.24	0.20/0.17
1	1	x	xz^2	1.97	2.10	1.68/-2.09
1	3	x	$x(3x^2-y^2)$		0.15	0.20/-0.01

D. Wavefunctions and Crystal Fields

In the following, we report the crystal-field splittings and wavefunctions of the ground-state multiplets, expressed in the total angular momentum $J = 3/2$ and $J = 2$ basis. One can observe that the relaxed geometry of the constrained supercell, in this case, together with the broken symmetry brought by the polaron localization, breaks the equivalence between in-plane and out-of-plane osmium sites as observed previously. This result impact on the MF calculation (see Fig. 9).

Energy (meV) for Os-1	
	0 7.2
$ 3/2, -3/2\rangle$	$1/\sqrt{2}$
$ 3/2, -1/2\rangle$	$1/\sqrt{2}$
$ 3/3, 1/2\rangle$	$1/\sqrt{2}$
$ 3/2, 3/2\rangle$	$1/\sqrt{2}$

Energy (meV) for Os-2					
	0	10.2	19.6	20.6	28.6
$ 2, -2\rangle$	0.590	0.388		$1/\sqrt{2}$	
$ 2, -1\rangle$			$-1/\sqrt{2}$		$1/\sqrt{2}$
$ 2, 0\rangle$	-0.550	0.835			
$ 2, 1\rangle$			$1/\sqrt{2}$		$1/\sqrt{2}$
$ 2, 2\rangle$	0.590	0.388		$-1/\sqrt{2}$	

Energy (meV) for Os-3					
	0	17.9	20.2	32.7	34.4
$ 2, -2\rangle$	$1/\sqrt{2}$	$1/\sqrt{2}$			
$ 2, -1\rangle$				$1/\sqrt{2}$	$1/\sqrt{2}$
$ 2, 0\rangle$			1		
$ 2, 1\rangle$				$1/\sqrt{2}$	$-1/\sqrt{2}$
$ 2, 2\rangle$	$1/\sqrt{2}$	$-1/\sqrt{2}$			

Energy (meV) for Os-4					
	0	1.7	13.7	14.2	15.9
$ 2, -2\rangle$		$1/\sqrt{2}$			$1/\sqrt{2}$
$ 2, -1\rangle$			$1/\sqrt{2}$	$-1/\sqrt{2}$	
$ 2, 0\rangle$	1				
$ 2, 1\rangle$			$1/\sqrt{2}$	$1/\sqrt{2}$	
$ 2, 2\rangle$		$1/\sqrt{2}$			$-1/\sqrt{2}$

Energy (meV) for Os-5					
	0	4.7	18.5	19.6	22.4
$ 2, -2\rangle$	0.655	-0.266	$1/\sqrt{2}$		
$ 2, -1\rangle$				$1/\sqrt{2}$	$1/\sqrt{2}$
$ 2, 0\rangle$	0.375	0.926			
$ 2, 1\rangle$				$1/\sqrt{2}$	$-1/\sqrt{2}$
$ 2, 2\rangle$	0.655	-0.266	$-1/\sqrt{2}$		

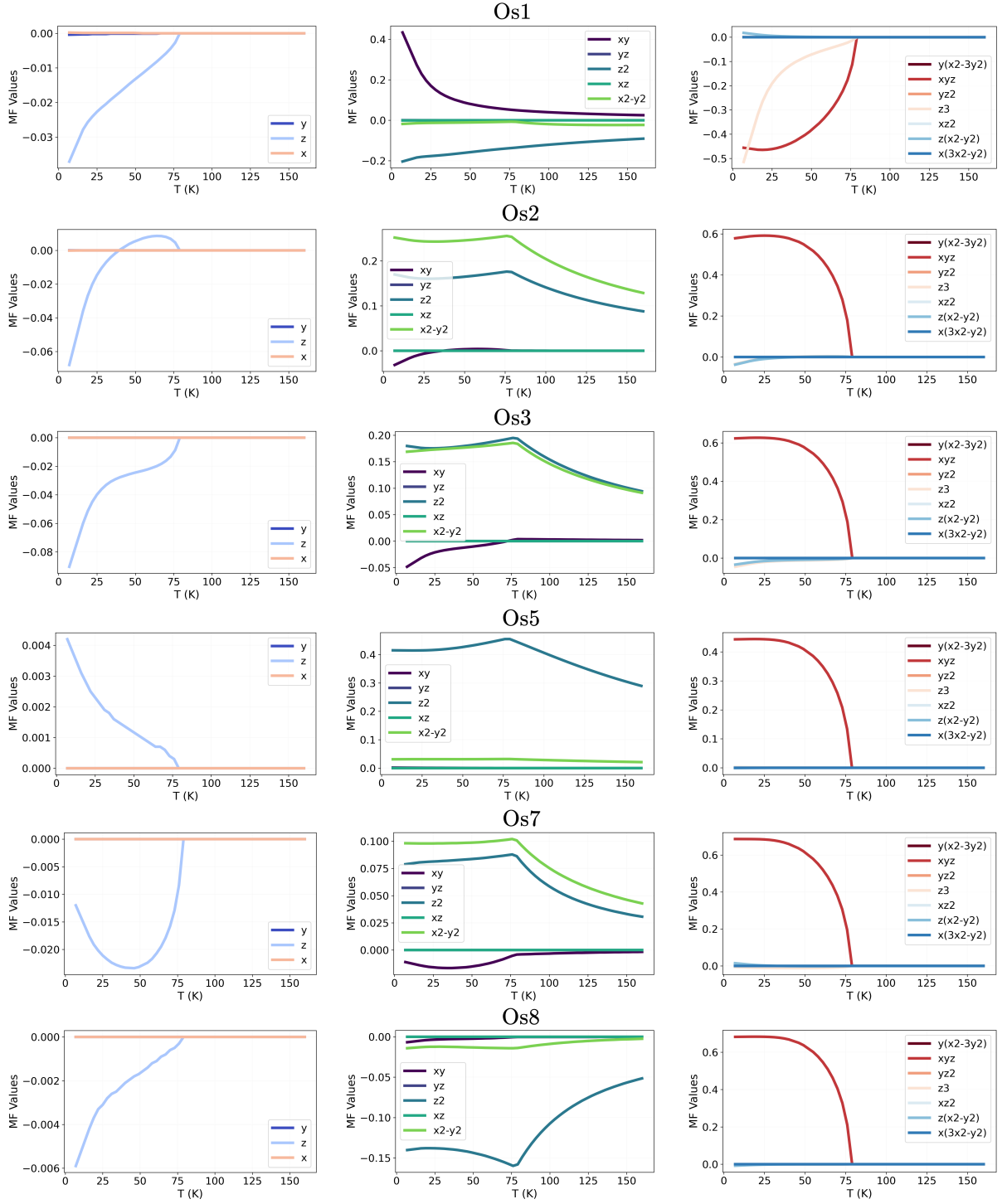
Energy (meV) for Os-6					
	0	3.4	18.5	18.8	21.1
$ 2, -2\rangle$	0.636	-0.307	$1/\sqrt{2}$		
$ 2, -1\rangle$				$1/\sqrt{2}$	$1/\sqrt{2}$
$ 2, 0\rangle$	0.435	0.900			
$ 2, 1\rangle$				$1/\sqrt{2}$	$-1/\sqrt{2}$
$ 2, 2\rangle$	0.636	-0.307	$-1/\sqrt{2}$		

Energy (meV) for Os-7					
	0	8.8	19.0	21.2	27.1
$ 2, -2\rangle$	0.648	-0.282	$1/\sqrt{2}$		
$ 2, -1\rangle$				$1/\sqrt{2}$	$1/\sqrt{2}$
$ 2, 0\rangle$	0.399	0.917			
$ 2, 1\rangle$				$1/\sqrt{2}$	$-1/\sqrt{2}$
$ 2, 2\rangle$	0.648	-0.282	$-1/\sqrt{2}$		

Energy (meV) for Os-7					
	0	10.5	20.0	20.8	29.1
$ 2, -2\rangle$	0.621	-0.338	$1/\sqrt{2}$		
$ 2, -1\rangle$				$1/\sqrt{2}$	$1/\sqrt{2}$
$ 2, 0\rangle$	0.478	0.878			
$ 2, 1\rangle$				$1/\sqrt{2}$	$-1/\sqrt{2}$
$ 2, 2\rangle$	0.621	-0.338	$-1/\sqrt{2}$		

E. Ordered Phase and Mean Field values with temperature

In Fig.9, we present the MF values of different multipolar operators in Cartesian coordinates. A sign reversal of the dominant octupolar exchange interaction occurs at $T_N \approx 77$ K. At higher temperatures, the only nonzero MF components are quadrupoles of z^2 and $x^2 - y^2$ character, consistent with the undistorted case. Importantly, in line with the constrained DFT+U result, the supercell exhibits a weak ferromagnetic moment of $\sim 0.02, \mu_B$. At low temperature, the ordered state involves the z^3 octupole, whose Γ_2 symmetry matches that of the dipoles (z). This behavior reflects a crystal-field effect: the presence of the polaron lowers nearby T_{2g} states sufficiently to favor z^3 ordering, even though the change in IEI relative to the undistorted case is not particularly strong (see Tab.II and Tab. III).

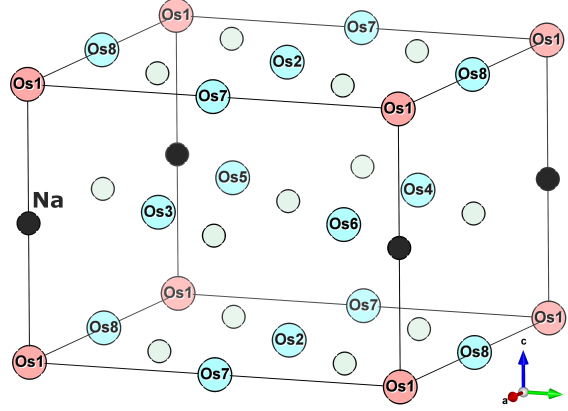


Supplementary Figure 9: MF values of multipolar operators O_K^Q expressed in Cartesian coordinates as a function of temperature for the different osmium ions of Fig. 6.

V. DOPING CONCENTRATION $\delta = 0.125$ WITH CHEMICAL DOPING

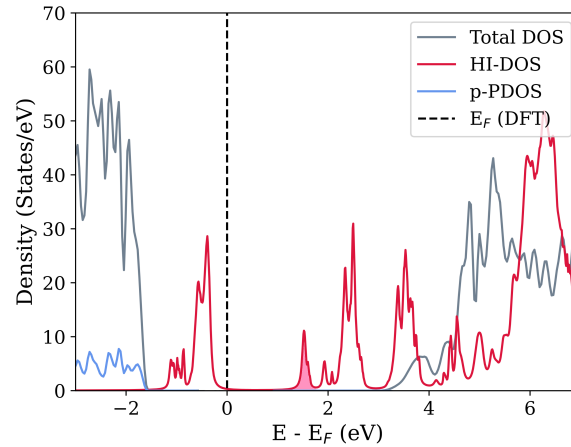
In the following, we present DFT+HI, FT-HI, and MF results for $\text{Ba}_2\text{Ca}_{1-\delta}\text{Na}_\delta\text{OsO}_6$ with chemical substitution of Ca with Na ions at doping concentration $\delta = 0.125$. Section A describes the structural details, Section B reports the DFT+HI density of states, Section C discusses the J_{eff} -IEI, Section D analyzes the crystal-field splittings and ground-state multiplet wavefunctions, and Section E presents the ordered phase and the MF order parameters as a function of temperature.

A. Structure



Supplementary Figure 10: Supercell of $\text{Ba}_2\text{Ca}_{1-\delta}\text{Na}_\delta\text{OsO}_6$ with labels for the osmium ions as indexed in the next Sections. The polaron is localized on the Os1 (light red).

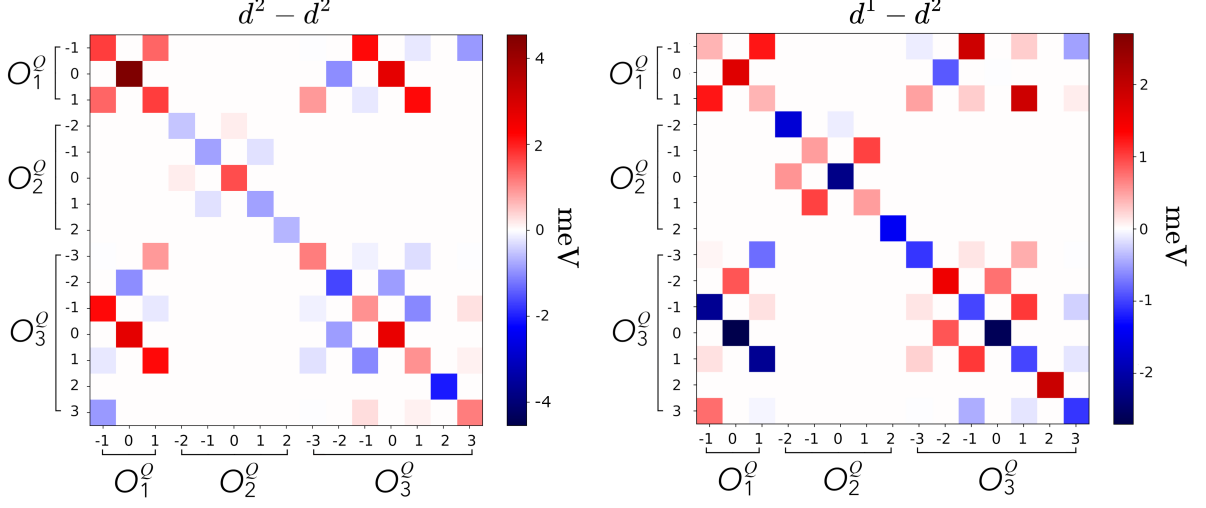
B. Polaronic density of States in DFT, DFT+HI



Supplementary Figure 11: Combined the DFT and DFT+HI DOS. The hole-polaron peak is highlighted in light-red.

C. Intersite Exchange Interactions in J_{eff} basis

In Suppl. Fig. 12, the IEI in $\text{Ba}_2\text{Ca}_{1-\delta}\text{Na}_\delta\text{OsO}_6$ are shown as a color map, with the corresponding values listed in Suppl. Table IV for the two cases of d^2-d^2 and d^1-d^2 electronic configurations. For the d^1-d^2 bond, an even stronger antisymmetric IEI matrix appears both in quadrupole-quadrupole and dipole-octupole interactions induced by the polaron.



Supplementary Figure 12: Color map of the IEI $V_{KK'}^{QQ'}$ in $\text{Ba}_2\text{Ca}_{1-\delta}\text{Na}_\delta\text{OsO}_6$ at pressure $[0,1/2,0]$ Os-Os pair for (left) $d^2 - d^2$ interaction and (right) $d^1 - d^2$ interaction. All values are in meV. The numerical list of $V_{KK'}^{QQ'}$ is given in Suppl. Table IV.

Supplementary Table IV: Calculated IEI $V_{KK'}^{QQ'}$ for the $J_{\text{eff}} = 3/2/J_{\text{eff}} = 2$ multiplets. The first two columns list Q and Q' , while the third and fourth columns display the KQ and $K'Q'$ tensors in Cartesian representation. The last three columns report the IEI values (in meV) for the $[0, 1/2, 0]$ nearest-neighbor Os–Os bond in the supercell reference frame, comparing: (i) d^2 – d^2 interactions from Ref.⁹, (ii) d^2 – d^2 interactions from this work, and (iii) d^1 – d^2 interactions from this work. A slash denotes the reversed Q/Q' case, highlighting the asymmetric contributions.

Bonds $\mathbf{R}_{ij} = [0.5, 0.5, 0]$ (primitive cell)				$d^2 - d^2$ (Ref. ⁹)	$d^2 - d^2$	$d^1 - d^2$
Dipole-Dipole						
-1	-1	y	y	1.62	1.73	0.40
0	0	z	z	4.17	4.55	1.68
1	-1	x	y	1.26	1.38	1.24
1	1	x	x	1.62	1.73	0.40
Quadrupole-Quadrupole						
-2	-2	xy	xy	-0.41	-0.52	-1.65
-1	-1	yz	yz	-0.79	-0.84	0.52
0	-2	z^2	xy	0.16	0.15	0.56/-0.09
0	0	z^2	z^2	1.32	1.59	-2.25
1	-1	xz	yz	-0.23	-0.26	1.01
1	1	xz	xz	-0.79	-0.84	0.52
2	2	x^2-y^2	x^2-y^2	-0.58	-0.67	-1.42
Octupole-Octupole						
-3	-3	$y(x^2-3y^2)$	$y(x^2-3y^2)$	1.16	1.15	-1.07
-2	-2	xyz	xyz	-1.49	-1.64	1.51
-1	-3	yz^2	$y(x^2-3y^2)$	-0.14	-0.13	0.15
-1	-1	yz^2	yz^2	0.80	0.96	-0.98
0	-2	z^3	xyz	-0.79	-0.87	0.74
0	0	z^3	z^3	2.35	2.66	-2.61
1	-3	xz^2	$y(x^2-3y^2)$	-0.29	-0.29	0.25/0.44
1	-1	xz^2	yz^2	-0.98	-1.05	1.04
1	1	xz^2	xz^2	0.80	0.96	-0.98
2	2	$z(x^2-y^2)$	$z(x^2-y^2)$	-1.89	-2.04	1.92
3	-1	$x(3x^2-y^2)$	yz^2	0.29	0.28	-0.25
3	1	$x(3x^2-y^2)$	xz^2	0.14	0.13	-0.14
3	3	$x(3x^2-y^2)$	$x(3x^2-y^2)$	1.16	1.15	-1.07
Dipole-Octupole						
-1	-3	y	$y(x^2-3y^2)$		-0.02	-0.10/0.06
-1	-1	y	yz^2	1.97	2.20	1.87/-2.17
-1	1	y	xz^2	-0.20	-0.20	0.26/0.17
-1	3	y	$x(3x^2-y^2)$	-0.89	-0.92	-0.50/0.78
0	-2	z	xyz	-0.97	-0.99	-0.88/0.89
0	0	z	z^3	2.38	2.71	-0.01/-2.71
0	2	z	$z(x^2-3y^2)$			
1	-3	x	$y(x^2-3y^2)$	0.89	0.92	0.50/-0.78
1	-1	x	yz^2	-0.20	-0.20	0.26/0.17
1	1	x	xz^2	1.97	2.21	1.87/-2.17
1	3	x	$x(3x^2-y^2)$		0.02	0.10/-0.06

D. Wavefunctions and Crystal Fields

In the following, we report the crystal-field splittings and wavefunctions of the ground-state multiplets, expressed in the total angular momentum $J = 3/2$ and $J = 2$ basis. As in Sec. III, the tetragonal symmetry of the chosen supercell and the broken symmetry brought by the polaron localization bring an equivalence between in-plane and out-of-plane osmium sites respectively. This feature manifests subsequently in the MF results (see Fig. 13).

Energy (meV) for Os-1	
	0 20.3
$ 3/2, -3/2\rangle$	$1/\sqrt{2}$
$ 3/2, -1/2\rangle$	$1/\sqrt{2}$
$ 3/3, 1/2\rangle$	$1/\sqrt{2}$
$ 3/2, 3/2\rangle$	$1/\sqrt{2}$

Energy (meV) for Os-2					
	0	0.9	17.4	17.5	17.5
$ 2, -2\rangle$		$1/\sqrt{2}$	$1/\sqrt{2}$		
$ 2, -1\rangle$					1
$ 2, 0\rangle$	1				
$ 2, 1\rangle$				1	
$ 2, 2\rangle$		$1/\sqrt{2}$	$1/\sqrt{2}$		

Energy (meV) for Os-3					
	0	14.8	15.2	26.4	28.8
$ 2, -2\rangle$	0.323	0.629			$1/\sqrt{2}$
$ 2, -1\rangle$			$1/\sqrt{2}$	$1/\sqrt{2}$	
$ 2, 0\rangle$	0.889	-0.457			
$ 2, 1\rangle$			$1/\sqrt{2}$	$-1/\sqrt{2}$	
$ 2, 2\rangle$	0.323	0.629			$-1/\sqrt{2}$

Energy (meV) for Os-4					
	0	14.8	15.2	26.4	28.8
$ 2, -2\rangle$	0.323	0.629			$1/\sqrt{2}$
$ 2, -1\rangle$			$1/\sqrt{2}$	$1/\sqrt{2}$	
$ 2, 0\rangle$	0.889	-0.457			
$ 2, 1\rangle$			$1/\sqrt{2}$	$-1/\sqrt{2}$	
$ 2, 2\rangle$	0.323	0.629			$-1/\sqrt{2}$

Energy (meV) for Os-5					
	0	14.8	15.2	26.4	28.8
$ 2, -2\rangle$	0.323	0.629			$1/\sqrt{2}$
$ 2, -1\rangle$			$1/\sqrt{2}$	$1/\sqrt{2}$	
$ 2, 0\rangle$	0.889	-0.457			
$ 2, 1\rangle$			$1/\sqrt{2}$	$-1/\sqrt{2}$	
$ 2, 2\rangle$	0.323	0.629			$-1/\sqrt{2}$

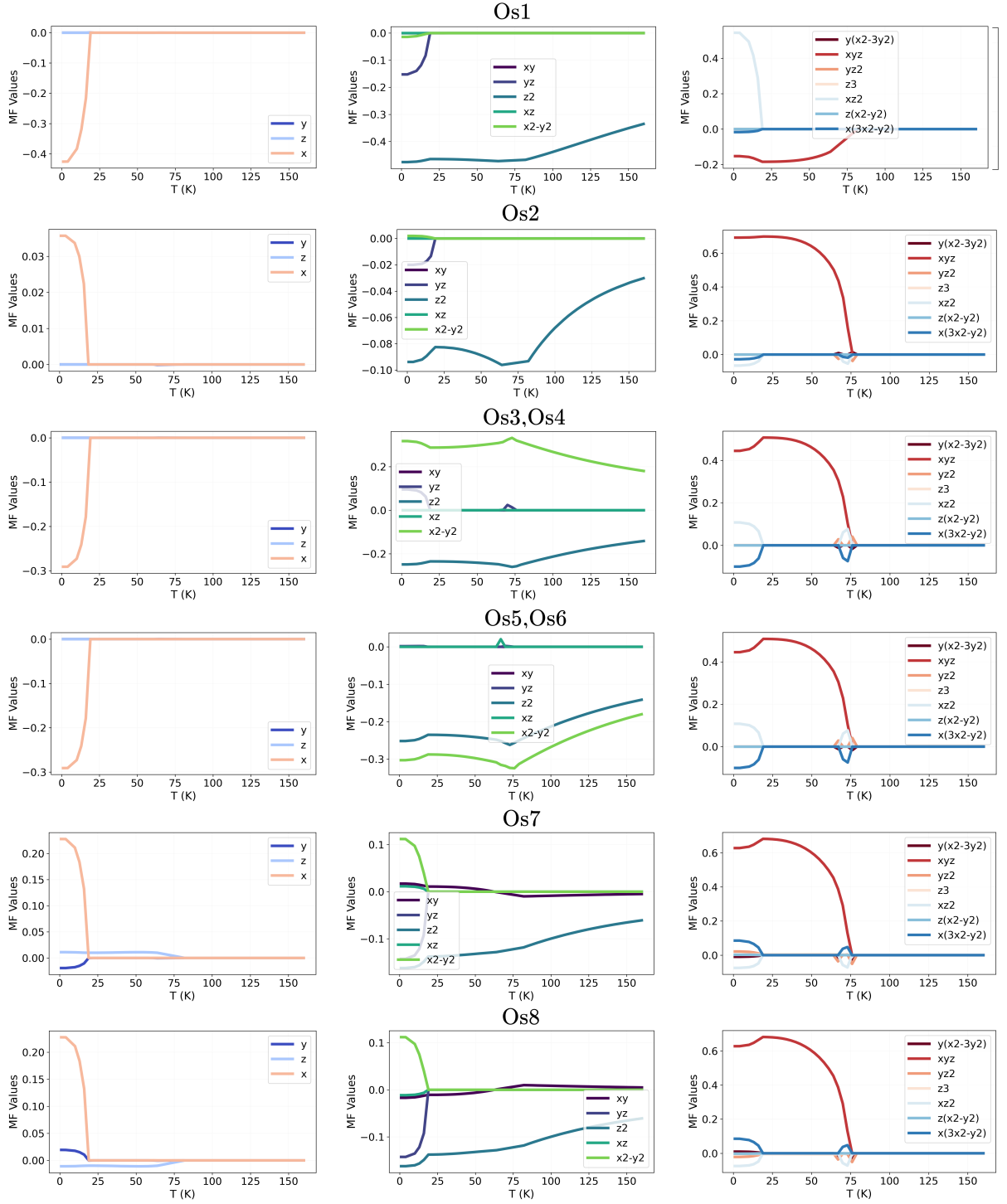
Energy (meV) for Os-6					
	0	14.8	15.2	26.4	28.8
$ 2, -2\rangle$	0.323	0.629			$1/\sqrt{2}$
$ 2, -1\rangle$			$1/\sqrt{2}$	$1/\sqrt{2}$	
$ 2, 0\rangle$	0.889	-0.457			
$ 2, 1\rangle$			$1/\sqrt{2}$	$-1/\sqrt{2}$	
$ 2, 2\rangle$	0.323	0.629			$-1/\sqrt{2}$

Energy (meV) for Os-7					
	0	3.6	18.2	18.2	20.3
$ 2, -2\rangle$		$1/\sqrt{2}$			$1/\sqrt{2}$
$ 2, -1\rangle$				1	
$ 2, 0\rangle$	1				
$ 2, 1\rangle$			1		
$ 2, 2\rangle$		$1/\sqrt{2}$			$-1/\sqrt{2}$

Energy (meV) for Os-7					
	0	3.6	18.2	18.2	20.3
$ 2, -2\rangle$		$1/\sqrt{2}$			$1/\sqrt{2}$
$ 2, -1\rangle$				1	
$ 2, 0\rangle$	1				
$ 2, 1\rangle$			1		
$ 2, 2\rangle$		$1/\sqrt{2}$			$-1/\sqrt{2}$

E. Ordered Phase and Mean Field values with temperature

In Fig. 5, we show the MF values of different multipolar operators in Cartesian coordinates. The sign reversal of the dominant octupolar exchange interaction remains present, although renormalized, and occurs at $T_N \approx 75$ K. At higher temperatures, only the quadrupoles of z^2 and $x^2 - y^2$ character acquire finite expectation values, consistent with the previous cases (See Fig. 5). However, in this chemically doped configuration a second transition is observed at lower temperature (~ 25 K), involving the simultaneous ordering of dipoles, quadrupoles, and octupoles. This transition is likely an artifact of the missing structural relaxation around the Na dopant, which is expected to significantly alter the local oxygen environment compared to the virtual-doping case discussed earlier. The spurious curves occurring around $T = 75$ K are a consequence of the poor MF convergence.



Supplementary Figure 13: MF values of multipolar operators O_K^Q expressed in Cartesian coordinates as a function of temperature for the different osmium ions of Fig. 10.

VI. CONSTRAINED DFT+U ODMS

In the following we report the ODMS used in the constrained DFT+U in the global reference frame of the supercell used, thus rotated by 45° with respect to the local octahedral reference frame.

A. Polaron (d^1)

spin component 1									
0.61788	0.00000	-0.00000	0.00000	0.00000	-0.00000	0.00000	-0.00158	0.00000	0.01615
0.00000	0.70678	0.00000	0.00001	0.00000	0.00000	0.00000	0.00000	0.08251	0.00000
-0.00000	0.00000	0.61789	0.00000	-0.01619	0.00158	0.00000	-0.00000	0.00000	0.00000
0.00000	0.00001	0.00000	0.41890	0.00000	0.00000	-0.08251	0.00000	-0.00000	0.00000
-0.00000	0.00000	-0.01619	0.00000	0.56195	-0.01615	0.00000	0.00000	0.00000	0.00000
spin component 2									
0.00000	0.00589	0.00000	0.00000	0.00000	0.00000	-0.00000	0.00000	-0.02213	0.00000
0.02213	0.00000	0.00000	0.00000	-0.00001	-0.00000	0.00000	-0.02219	0.00000	-0.22612
0.00000	-0.00000	0.00000	0.02219	0.00000	0.00000	0.00591	0.00000	-0.00000	0.00000
-0.00000	0.00000	-0.00591	0.00000	-0.06021	-0.00589	0.00000	-0.00000	0.00000	0.00000
0.00000	0.00000	0.00000	-0.22612	0.00000	0.00000	-0.06021	0.00000	-0.00001	0.00000
spin component 3									
0.00000	0.02213	0.00000	0.00000	0.00000	0.00000	-0.00000	0.00000	0.00589	0.00000
0.00589	0.00000	-0.00000	0.00000	0.00000	-0.00000	0.00000	-0.00591	0.00000	0.06021
0.00000	-0.00000	0.00000	-0.00591	0.00000	0.00000	0.02219	0.00000	-0.00000	0.00000
0.00000	0.00000	0.02219	0.00000	-0.22612	0.02213	0.00000	-0.00000	0.00000	0.00001
0.00000	-0.00001	0.00000	-0.06021	0.00000	0.00000	0.22612	0.00000	-0.00000	0.00000
spin component 4									
0.61788	0.00000	0.00000	0.00000	0.00000	0.00000	0.00000	-0.00158	0.00000	-0.01615
0.00000	0.41890	0.00000	0.00001	0.00000	0.00000	-0.00000	0.00000	-0.08251	0.00000
0.00000	0.00000	0.61789	0.00000	-0.01619	0.00158	0.00000	0.00000	0.00000	0.00000
0.00000	0.00001	0.00000	0.70678	0.00000	0.00000	0.08251	0.00000	-0.00000	0.00000
-0.00000	0.00000	0.01619	0.00000	0.56195	0.01615	0.00000	0.00000	0.00000	-0.00000

B. d^2

spin component 1									
0.57623	0.00000	-0.00000	0.00000	-0.00000	0.00000	0.00000	-0.00566	0.00000	0.03559
0.00000	0.82697	0.00000	-0.00016	0.00000	0.00000	-0.00000	0.00000	0.12984	0.00000
0.00000	0.00000	0.57630	0.00000	-0.04117	0.00566	0.00000	-0.00000	0.00000	-0.00002
0.00000	-0.00016	0.00000	0.36763	0.00000	0.00000	-0.12984	0.00000	0.00000	0.00000
0.00000	0.00000	-0.04117	0.00000	0.59576	-0.03559	0.00000	0.00002	0.00000	0.00000
spin component 2									
0.00000	0.01762	0.00000	-0.00000	0.00000	0.00000	-0.00000	0.00000	-0.05326	0.00000
0.05326	0.00000	0.00002	0.00000	0.00013	-0.00000	0.00000	-0.05180	0.00000	-0.35948
0.00000	-0.00002	0.00000	0.05180	0.00000	0.00000	0.01050	0.00000	-0.00002	0.00000
0.00000	0.00000	-0.01050	0.00000	-0.09904	-0.01762	0.00000	0.00002	0.00000	-0.00013
0.00000	-0.00013	0.00000	-0.35948	0.00000	0.00000	-0.09904	0.00000	0.00013	0.00000
spin component 3									
0.00000	0.05326	0.00000	-0.00000	0.00000	0.00000	0.00000	0.00000	0.01762	0.00000
0.01762	0.00000	-0.00002	0.00000	-0.00013	-0.00000	0.00000	-0.01050	0.00000	0.09904
0.00000	0.00002	0.00000	-0.01050	0.00000	0.00000	0.05180	0.00000	-0.00002	0.00000
0.00000	0.00000	0.05180	0.00000	-0.35948	0.05326	0.00000	0.00002	0.00000	-0.00013
0.00000	0.00013	0.00000	-0.09904	0.00000	0.00000	0.35948	0.00000	0.00013	0.00000
spin component 4									
0.57623	0.00000	0.00000	0.00000	-0.00000	-0.00000	0.00000	-0.00566	0.00000	-0.03559
0.00000	0.36763	0.00000	-0.00016	0.00000	0.00000	0.00000	0.00000	-0.12984	0.00000
-0.00000	0.00000	0.57630	0.00000	0.04117	0.00566	0.00000	0.00000	0.00000	0.00002
0.00000	-0.00016	0.00000	0.82697	0.00000	0.00000	0.12984	0.00000	-0.00000	0.00000
0.00000	0.00000	0.04117	0.00000	0.59576	0.03559	0.00000	-0.00002	0.00000	-0.00000

-
- ¹ P Blaha, K Schwarz, G Madsen, D Kvasnicka, J Luitz, R Laskowski, F Tran, and L D. Marks, *WIEN2k, An augmented Plane Wave + Local Orbitals Program for Calculating Crystal Properties* (Karlheinz Schwarz, Techn. Universität Wien, Austria, ISBN 3-9501031-1-2, 2018).
- ² A. Georges, G. Kotliar, W. Krauth, and M. J. Rozenberg, “Dynamical mean-field theory of strongly correlated fermion systems and the limit of infinite dimensions,” *Rev. Mod. Phys.* **68**, 13–125 (1996).
- ³ V I Anisimov, A I Poteryaev, M A Korotin, A O Anokhin, and G Kotliar, “First-principles calculations of the electronic structure and spectra of strongly correlated systems: dynamical mean-field theory,” *Journal of Physics: Condensed Matter* **9**, 7359 (1997).
- ⁴ A. I. Lichtenstein and M. I. Katsnelson, “Ab initio calculations of quasiparticle band structure in correlated systems: LDA++ approach,” *Phys. Rev. B* **57**, 6884–6895 (1998).
- ⁵ M. Aichhorn, L V. Pourovskii, P. Seth, V. Vildosola, M. Zingl, O. E Peil, X. Deng, J. Mravlje, G. J Krabberger, C. Martins, *et al.*, “TRIQS/DFTTools: A TRIQS application for ab initio calculations of correlated materials,” *Computer Physics Communications* **204**, 200–208 (2016).
- ⁶ J. Hubbard, “Electron correlations in narrow energy bands,” *Proc. Roy. Soc. (London)* **A 276**, 238 (1963).
- ⁷ C M Thompson, J P Carlo, R Flacau, T Aharen, I A Leahy, J R Pollichiemi, T J S Munsie, T Medina, G M Luke, J Munevar, S Cheung, T Goko, Y J Uemura, and J E Greedan, “Long-range magnetic order in the $5d^2$ double perovskite $\text{Ba}_2\text{CaOsO}_6$: comparison with spin-disordered Ba_2YReO_6 ,” *Journal of Physics: Condensed Matter* **26**, 306003 (2014).
- ⁸ D. Fiore Mosca, L V. Pourovskii, B. H. Kim, P. Liu, S. Sanna, F. Boscherini, S. Khmelevskiy, and C. Franchini, “Interplay between multipolar spin interactions, jahn-teller effect, and electronic correlation in a $J_{\text{eff}} = \frac{3}{2}$ insulator,” *Phys. Rev. B* **103**, 104401 (2021).
- ⁹ L V. Pourovskii, D. Fiore Mosca, and C. Franchini, “Ferro-octupolar order and low-energy excitations in d^2 double perovskites of osmium,” *Phys. Rev. Lett.* **127**, 237201 (2021).
- ¹⁰ L V. Pourovskii, “Two-site fluctuations and multipolar intersite exchange interactions in strongly correlated systems,” *Phys. Rev. B* **94**, 115117 (2016).
- ¹¹ L V. Pourovskii, “Multipolar interactions and magnetic excitation gap in d^3 spin-orbit Mott insulators,” *Phys. Rev. B* **108**, 054436 (2023).
- ¹² Dario Fiore Mosca, Leonid V. Pourovskii, and Cesare Franchini, “Modeling magnetic multipolar phases in density functional theory,” *Phys. Rev. B* **106**, 035127 (2022).
- ¹³ S. Agrestini, F. Borgatti, P. Florio, J. Frassinetti, D. Fiore Mosca, Q. Faure, B. Detlefs, C. J. Sahle, S. Francoual, J. Choi, M. Garcia-Fernandez, K.-J. Zhou, V. F. Mitrović, P. M. Woodward, G. Ghiringhelli, C. Franchini, F. Boscherini, S. Sanna, and M. Moretti Sala, “Origin of magnetism in a supposedly nonmagnetic osmium oxide,” *Phys. Rev. Lett.* **133**, 066501 (2024).
- ¹⁴ G. Kresse and J. Furthmüller, “Efficient iterative schemes for ab initio total-energy calculations using a plane-wave basis set,” *Phys. Rev. B* **54**, 11169–11186 (1996).
- ¹⁵ G. Kresse and J. Hafner, “Ab initio molecular dynamics for liquid metals,” *Phys. Rev. B* **47**, 558–561 (1993).
- ¹⁶ A. I. Liechtenstein, V. I. Anisimov, and J. Zaanen, “Density-functional theory and strong interactions: Orbital ordering in mott-hubbard insulators,” *Phys. Rev. B* **52**, R5467–R5470 (1995).
- ¹⁷ Oleksandr I. Malyi and Alex Zunger, “False metals, real insulators, and degenerate gapped metals,” *Applied Physics Reviews* **7**, 041310 (2020).
- ¹⁸ Bongjae Kim, Peitao Liu, Zeynep Ergönenc, Alessandro Toschi, Sergii Khmelevskiy, and Cesare Franchini, “Lifshitz transition driven by spin fluctuations and spin-orbit renormalization in NaOsO_3 ,” *Phys. Rev. B* **94**, 241113 (2016).
- ¹⁹ Peitao Liu, Jiangang He, Bongjae Kim, Sergii Khmelevskiy, Alessandro Toschi, Georg Kresse, and Cesare Franchini, “Comparative ab initio study of the structural, electronic, magnetic, and dynamical properties of LiOsO_3 and NaOsO_3 ,” *Phys. Rev. Mater.* **4**, 045001 (2020).
- ²⁰ Dario Fiore Mosca, Hermann Schnait, Lorenzo Celiberti, Markus Aichhorn, and Cesare Franchini, “The Mott transition in the $5d^1$ compound $\text{Ba}_2\text{NaOsO}_6$: A DFT+DMFT study with PAW spinor projectors,” *Computational Materials Science* **233**, 112764 (2024).
- ²¹ A Mansouri Tehrani and N A. Spaldin, “Untangling the structural, magnetic dipole, and charge multipolar orders in $\text{Ba}_2\text{MgReO}_6$,” *Phys. Rev. Mater.* **5**, 104410 (2021).